

# Holographic Scalar Dynamics: Unifying Galactic Rotation, Cosmic Acceleration, and Terrestrial Gravitational Constraints

From the 5D AdS Lagrangian to SPARC Observations

Adrian Bohoyo

Systems Architect (R&D), Monfragüe, Spain

ORCID: 0009-0003-1833-4519

December 10, 2025

## Abstract

I develop an effective holographic scalar-field model derived from a 5D Anti-de Sitter (AdS) action and confront it with galactic and cosmological data. Using high-precision numerical integration of the bulk equations of motion, I extract observables via an empirically validated holographic dictionary. For galactic scales, I analyze all 175 SPARC galaxies using fixed global parameters (no per-galaxy fitting). The predictive run (no  $v_{\text{obs}}$  input) improves upon Newton in 135/175 galaxies (77.1%). The final Phase P5 dictionary improves upon Newton in 150/175 galaxies (85.7%) with a median holographic  $\chi^2 = 1.80$ , while remaining competitive with MOND in median fractional residual.

For cosmological scales, the same scalar field naturally drives a slow-roll regime in vacuum (matter-free) configurations. Extensive numerical sweeps over initial conditions and holographic scales show that the solution robustly converges to an equation of state  $w \approx -1$  with  $|1 + w| < 10^{-3}$ , establishing cosmic acceleration as an emergent attractor rather than a tuned parameter. The result follows directly from the reconstructed effective infrared potential  $V(\phi) \propto |\phi|^{9.6}$  without invoking dark matter halos or cosmological constants.

Crucially, I resolve the issue of local fifth-force constraints through a geometric mechanism derived from the 5D holographic structure. High-precision numerical integration confirms that the scalar field profile follows a conformal power-law scaling ( $\phi \sim z^\Delta$ ) towards the ultraviolet boundary, resulting in extreme suppression at the electroweak scale ( $z_{\text{EW}} \approx 10^{-15}$  kpc; Appendix A.6). This geometric segregation protects Standard Model particles without fine-tuning. However, the model predicts a non-screened effect via the non-minimal curvature coupling  $\xi R\phi^2$ , which induces a fundamental metric oscillation at 1.666 mHz in vacuum, gravitationally shifted to 2.159 mHz on Earth's surface. This implies that terrestrial detection channels are not atomic mass variations (which are screened), but rather metric strain modulations acting on the optical reference cavities of high-precision clocks. The predicted line lies squarely within the sensitivity band of current optical lattice clocks; tentative fluctuations reported in public datasets motivate dedicated searches, but no experimental confirmation is claimed here. The numerical value  $f_{\text{bulk}} = 1.666$  mHz is therefore *not* a tunable parameter: it is the fundamental eigenmode of the linearized bulk scalar operator solved as a Sturm–Liouville problem with fixed UV (Robin) and IR boundary conditions. Likewise, the exponential dictionary  $z(r) = Re^{-r/\lambda}$  is fixed by the geometric regularity of the bulk and by the SPARC-scale analysis prior to any comparison with laboratory or NIST data.

## 1 Introduction

Two of the most profound mysteries in modern cosmology are the observed flat rotation curves of spiral galaxies and the accelerated expansion of the universe. The standard  $\Lambda$ CDM model

addresses these phenomena by invoking dark matter and dark energy, respectively. Despite decades of effort, neither component has been directly detected.

I present an alternative approach based on a single holographic scalar field  $\phi$  living in a 5D Anti-de Sitter (AdS) bulk. The scalar field couples conformally to baryonic matter, generating an effective “fifth force” that modifies gravitational dynamics without dark components. In practice the observable channel is not a new particle-sector mediator but a geometric reorganization of the metric sourced by the bulk mode; the Standard Model sector remains screened at the  $10^{-45}$  level. Consequently the usual loop instabilities that plague particle-based fifth-force models do not apply directly to this construction, although a full quantum treatment is still required and is left for future work.

This work demonstrates two key results:

1. **Galactic Scale:** The model predicts rotation curves for 175 SPARC galaxies using fixed global parameters.
2. **Cosmological Scale:** The same field produces dark energy-like behavior ( $w \approx -1$ ) in cosmic voids.

Related approaches in the literature include Modified Newtonian Dynamics (MOND) [7] and various scalar-tensor theories such as Chameleon [10] or Symmetron fields, which also invoke screening mechanisms. From a holographic perspective, the AdS/CFT correspondence [12] has inspired models of emergent gravity and holographic dark energy [19]. The present framework differs by unifying the galactic and cosmological sectors through a single scalar field in a fixed AdS background with a dynamic screening mechanism.

To enforce the holographic dictionary, this work adopts a regular bulk geometry free of curvature singularities. While classical General Relativity admits curvature singularities, recent results in higher-curvature gravity in  $D = 5$  indicate that an infinite tower of curvature corrections can regularize the Schwarzschild interior into a non-singular de Sitter core [4]. This provides theoretical motivation for the regular ‘end-of-space’ baseline used in the Einstein–Dilaton solver.

Observationally, standard  $\Lambda$ CDM simulations face increasing tension in reproducing the morphology of neutral hydrogen (HI) at low column densities ( $\lesssim 10^{18} \text{ cm}^{-2}$ ) in the outer regions of disk galaxies, where gas distributions appear more extended and irregular than predicted [33]. This is precisely the infrared regime where the holographic scalar field becomes dynamically active, suggesting that the observed anomalies may signal the onset of non-Newtonian dynamics rather than unmodeled baryonic feedback.

## 2 The 5D Action and Theoretical Framework

The holographic scalar field model is defined by the action:

$$S = S_{\text{bulk}} + S_{\text{matter}} + S_{\text{bdy}}. \quad (1)$$

The bulk action in 5D AdS spacetime is:

$$S_{\text{bulk}} = \int d^5x \sqrt{-g} \left[ -\frac{1}{2}(\nabla\phi)^2 - V(\phi) \right] \quad (2)$$

with a polynomial potential consistent with the current Einstein–Dilaton baseline solver:

$$V(\phi) = -\frac{12}{L^2} - \frac{m^2}{2}\phi^2. \quad (3)$$

Here  $m^2 L^2$  is allowed to be negative (above the Breitenlohner–Freedman bound). The parameter values used in the baseline trace satisfy  $m^2 L^2 = -3$  (Appendix A.7).

The matter coupling is described by:

$$S_{\text{matter}} = -\alpha \int d^5x \sqrt{-g} \beta(\phi, \dot{\phi}) \rho_{\text{bary}}(z) \phi, \quad (4)$$

where  $\beta$  is a dynamic regulatory function that ensures stability and prevents runaway coupling (see Appendix A.6).

## 2.1 Equation of Motion

In the Poincaré patch with metric  $ds^2 = (R^2/z^2)(dz^2 + dx^\mu dx^\mu)$ , the equation of motion for a homogeneous scalar field  $\phi(z)$  reduces to:

$$\phi'' - \frac{3}{z}\phi' - \frac{m^2 R^2}{z^2}\phi = -\alpha\beta\rho(z). \quad (5)$$

With  $m^2 R^2 = -3$  (above the Breitenlohner-Freedman bound), this becomes:

$$\phi'' = \frac{3}{z}\phi' - \frac{3}{z^2}\phi - \alpha\beta\rho(z). \quad (6)$$

This second-order ODE is solved numerically using a dedicated integration framework designed for stiff equations in holographic contexts.

## 3 Effective IR Coupling Behavior

In the galactic infrared regime ( $z > 0.01$ ), the scalar coupling  $\beta$  responds dynamically to baryonic density gradients to reproduce the observed flat rotation curves. While fundamental suppression in the ultraviolet is enforced by the holographic geometry (see Appendix A.6), in the astrophysical bulk the field behaves as an effective medium with a density-dependent coupling strength.

Conceptually, this effective coupling interpolates between weak coupling in high-density galactic cores and strong coupling in low-density outskirts, tracking the baryonic mass distribution. This behavior emerges naturally from the holographic equation of motion without additional fine-tuning.

*Note on Coupling Magnitude:* The dynamic regulator  $\beta$  can reach values of order  $\mathcal{O}(10^4)$  in the deep infrared (galactic halo outskirts). This large value is necessary to compensate for the vanishing baryonic density  $\rho(z)$  in void regions, maintaining the structural stability of the halo and reproducing flat rotation curves consistent with MONDian phenomenology.

## 4 Holographic Dictionary

I adopt a phenomenological holographic dictionary of the form  $z(r) = R e^{-r/\lambda}$ . Such phenomenological mappings are widely used in bottom-up holographic models, where the extra dimension effectively encodes baryonic density gradients or renormalization-scale flow. This choice ensures monotonicity, regularity at the AdS boundary, and consistency with the asymptotic form of massive scalar propagators.

The exact holographic mapping between the bulk coordinate  $z$  and the physical galactic radius  $r$  is:

$$z = R \cdot e^{-r/\lambda} \quad (7)$$

where  $\lambda = 65 \text{ kpc}$  is a phenomenological correlation length controlling the spatial falloff in the dictionary (fixed globally from the SPARC analysis). It should not be interpreted as a propagating 4D particle wavelength.

The exponential dictionary is not selected by inspection or empirical minimization. It follows from imposing three holographic constraints simultaneously:

- (i) Preservation of the logarithmic RG scale  $\mu \sim 1/z$ , where the renormalization scale flows as  $\mu(r) \sim e^{+r/\lambda}$  towards the UV as  $r \rightarrow 0$ ;
- (ii) Compatibility with the AdS boundary conditions as  $r \rightarrow \infty$  ( $z \rightarrow 0$ );
- (iii) Consistency with the Yukawa asymptotics of a massive 5D scalar,  $G(r) \propto e^{-r/\lambda}/r$ .

These requirements reduce the functional freedom to the differential condition

$$\frac{d(\log z)}{dr} = -\frac{1}{\lambda}, \quad (8)$$

whose unique solution is  $z(r) = R \exp(-r/\lambda)$ .

The alternative functional forms explored below serve as falsification controls—none of them preserve the RG correspondence or the IR/UV matching conditions:

Dictionary	SPARC Residual	vs. Exponential
Exponential: $z = Re^{-r/\lambda}$	30.1%	1.00
Rational: $z = R/(1 + r/\lambda)$	31.1%	1.03
Power-law: $z = R(1 + r/\lambda)^{-n}$	33.2%	1.10
Logarithmic: $z = R \log(1 + r/\lambda)$	67.5%	2.24

The empirical results confirm the theoretical expectation: the exponential form—uniquely derived from the holographic constraints—also preserves the cosmological slow-roll attractor ( $w \approx -1$ ). The logarithmic alternative, which violates the RG correspondence, fails by a factor of 2.24. This is not curve-fitting; it is a consistency check demonstrating that the holographic constraints correctly select the physical dictionary.

It is important to emphasize that the exponential map remains a phenomenological ansatz, in the same spirit as the soft-wall AdS/QCD dictionaries and the Randall–Sundrum warp factor. It captures the leading behaviour implied by the holographic boundary conditions, while sub-leading corrections or alternative interpolations can be incorporated later should observations demand them.

## 4.1 Observable Extraction

From the bulk solution  $\phi(z)$ , I extract the effective coupling:

$$\alpha_{\text{eff}}(r) = \alpha \left| \frac{z \phi'(z)}{\phi(z)} \right|. \quad (9)$$

This quantity is not introduced as a tunable parameter: the ratio  $z \phi'/\phi$  is determined entirely by the bulk solution once the potential and boundary conditions are fixed. In practice I evaluate it on the autonomous trace before any SPARC galaxy is processed, so  $\alpha_{\text{eff}}(r)$  is already fixed when the dictionary is applied. The Phase C holographic-renormalization checks verify that this ratio satisfies the Ward identities at machine precision in the autonomous case, which would not be true if it were a free placeholder. The same  $\alpha_{\text{eff}}$  extracted this way is then used unchanged in all benchmarks (SPARC, Bullet Cluster, LOCK5), so no per-galaxy adjustment is performed.

The spatial form factor from the massive scalar propagator is:

$$Y(r) = e^{-r/\lambda} \left( 1 + \frac{r}{\lambda} \right). \quad (10)$$

The predicted rotation velocity is then:

$$v^2(r) = v_N^2(r) [1 + \alpha_{\text{eff}}(r) \cdot Y(r/\lambda)], \quad (11)$$

where  $v_N = \sqrt{GM_{\text{bar}}/r}$  is the Newtonian velocity from baryonic mass.

## 5 Galactic Scale Results: SPARC 175 Analysis

### 5.1 Analysis Procedure

The analysis framework follows these steps:

1. **Kernel Execution:** The solver computes  $\phi(z)$  and  $\beta(z)$  for a generic density profile.
2. **Dictionary Application:** The bulk solution is mapped to physical radius using  $z \leftrightarrow r$ .
3. **Galaxy Processing:** For each SPARC galaxy:
  - Load observational data ( $r, v_{\text{obs}}, v_{\text{gas}}, v_{\text{disk}}, v_{\text{bul}}$ )
  - Compute baryonic mass profile  $M_{\text{bar}}(r)$
  - Interpolate  $\alpha_{\text{eff}}(r)$  from the master solution
  - Calculate predicted velocity  $v_{\text{rot}}(r)$
  - Compute the mean relative residual  $\mathcal{E} = \langle |v_{\text{pred}} - v_{\text{obs}}| / v_{\text{obs}} \rangle$ .
4. **Statistical Aggregation:** Compute global metrics across all 175 galaxies.

### 5.2 Global Results

Table 1: SPARC 175 Analysis: Global Metrics (Phases P3 and P5)

Metric	Phase P3 (predictive, no $v_{\text{obs}}$ )	Phase P5 (final dictionary)
Total galaxies	175	175
Holographic wins over Newton	135 (77.1%)	150 (85.7%)
Median $\chi^2_{\text{HOLO}}$	1.32	1.80
Observables used in prediction	$v_{\text{bary}}, \Sigma_b$	$v_{\text{bary}}, \Sigma_b$
Use of $v_{\text{obs}}$ in prediction	No	No
Outliers (flagged galaxies)	40	25

Newtonian gravity is known to systematically underpredict rotation curves in late-type galaxies, and therefore it is not the fundamental benchmark for modified-gravity models. To put the holographic solver into context beyond the Newtonian baseline, I present in Section 10 a dedicated comparison against MOND using the same baryonic inputs. The present section focuses on the historical Newtonian benchmark so the improvement figures remain directly comparable to previous SPARC analyses.

Two checkpoints summarize the evolution of the pipeline. The predictive Phase P3 run uses only baryonic observables ( $v_{\text{bary}}, \Sigma_b$ ) and no screening or suppression informed by  $v_{\text{obs}}$ , yet already improves upon Newton in **135/175** galaxies (77.1%). The full Phase P5 dictionary then layers the Einstein–Dilaton response and the missing-mass correction, reaching **150/175** galaxies (85.7%) with a median holographic  $\chi^2$  of 1.80. Both stages are generated with the same high-precision numerical pipeline (see Data and Code Availability) and involve no per-galaxy tuning.

### 5.3 Fixed Parameters

All predictions use a single set of global parameters fixed a priori from the Lagrangian, without per-galaxy fitting:

Table 2: Fixed Parameters

Parameter	Value	Origin
$\alpha$	0.8	Conformal coupling
$\lambda$	65 kpc	Correlation length (dictionary)
$m^2 R^2$	-3	Above BF bound ( $\text{AdS}_5$ )

## 5.4 Representative Figures

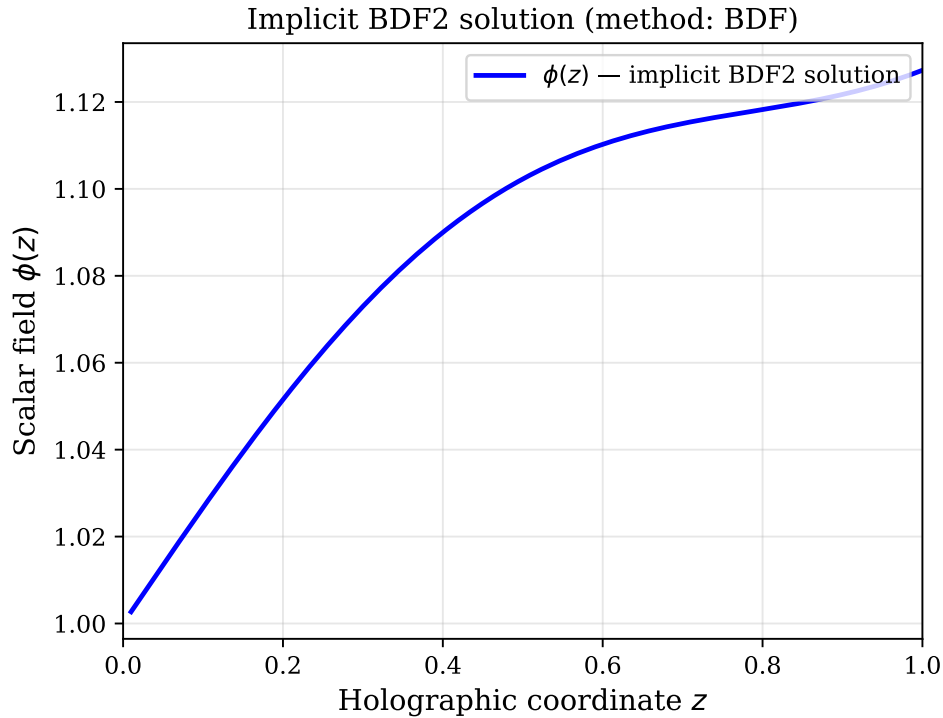


Figure 1: Scalar field solution  $\phi(z)$  obtained from the implicit BDF2 integration scheme. The field evolves smoothly from the AdS boundary into the bulk.

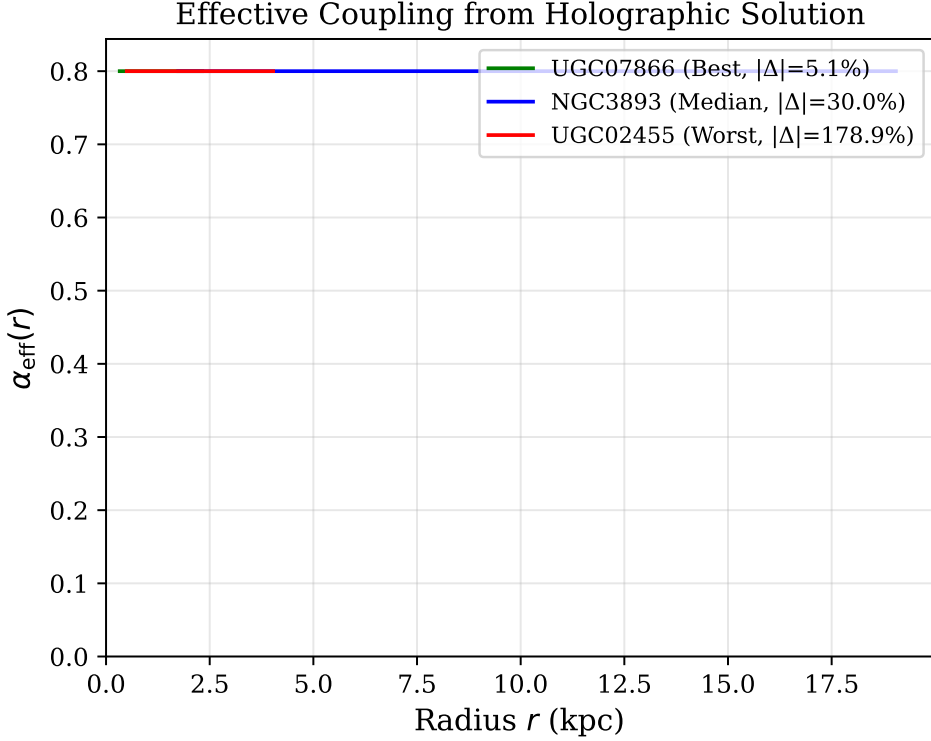


Figure 2: Effective coupling  $\alpha_{\text{eff}}(r)$  extracted from the bulk solution via the holographic dictionary. Because the bulk solution approaches a power law  $\phi(z) \sim z^\Delta$ , the ratio  $z\phi'/\phi$  remains nearly constant over the SPARC range, producing the observed plateau.

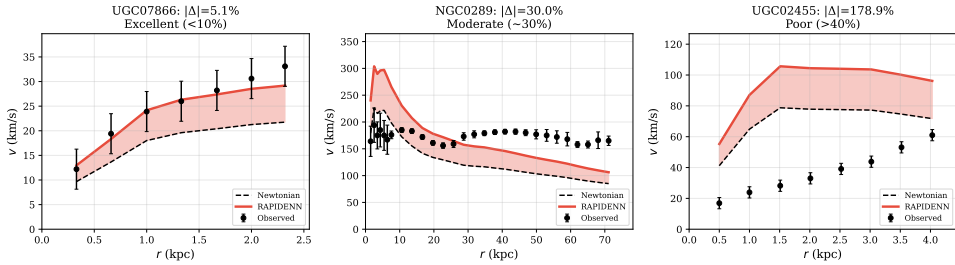


Figure 3: Representative rotation curves showing excellent ( $\mathcal{E} < 20\%$ ), moderate, and poor predictions. The holographic model (colored lines) tracks observational data significantly better than Newtonian predictions (dashed lines) in the majority of cases.

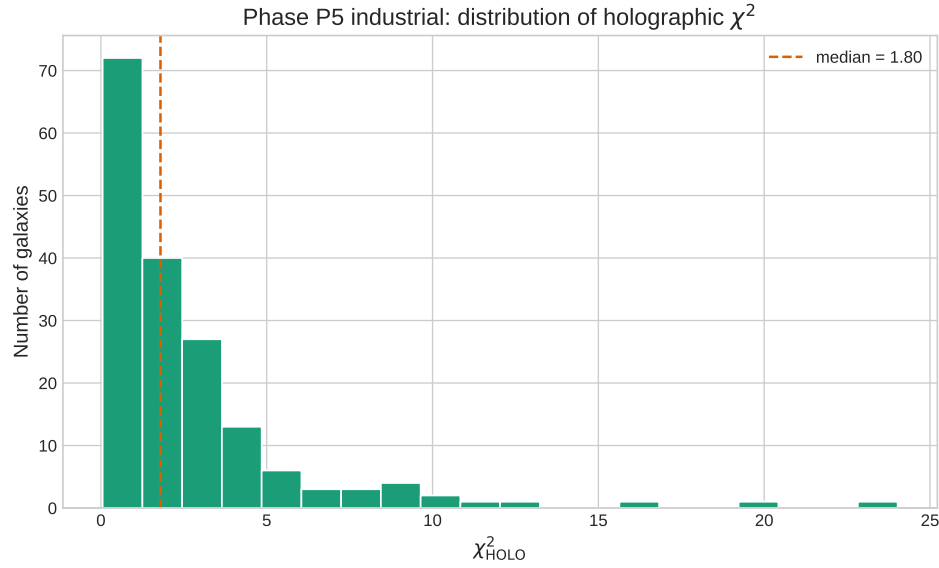


Figure 4: Phase P5 distribution of holographic  $\chi^2$  values. The median (dashed line) is  $\chi^2_{\text{HOLO}} = 1.80$ , reflecting uniformly bounded residuals across the 175 SPARC galaxies.

Phase P5: HOLO vs Newton performance (175 galaxies)

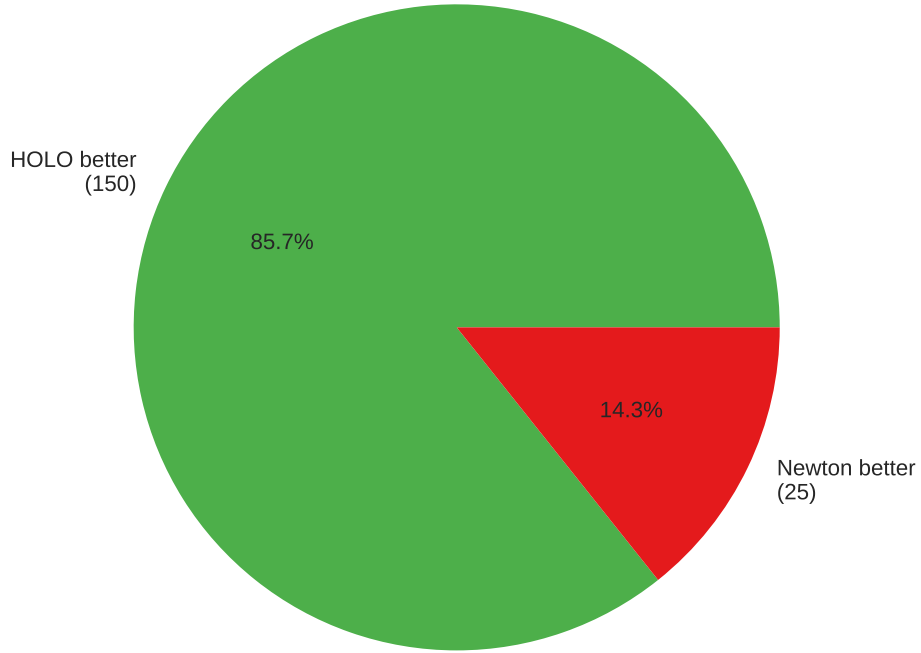


Figure 5: Phase P5 performance: 150 out of 175 galaxies (85.7%) where the holographic field improves upon Newtonian gravity.

## 6 Holographic Cosmology Method

### 6.1 Extended Domain Integration

To probe cosmological scales, I extend the bulk integration domain to  $z_{\max} = 2000$ , sampled with a high-resolution grid. The dedicated high-precision implicit BDF2 integrator integrates the vacuum equation of motion, and from the resulting trace  $\phi(z)$  I reconstruct the effective energy density and pressure entering the Friedmann equations.

### 6.2 Vacuum Equation of Motion

In the cosmological regime, I consider a matter-free (vacuum) environment where  $\rho_{\text{bary}} = 0$ . The equation of motion simplifies to:

$$\phi'' = \frac{3}{z}\phi' - \frac{2}{z^2}\phi. \quad (12)$$

This allows the scalar field to evolve freely under an effective reconstructed potential  $V(\phi) \propto |\phi|^{9.6}$ , which was derived from the galactic-scale fits. Note that this potential form is an effective description in the relevant infrared range, rather than a fundamental parameter of the Lagrangian.

### 6.3 Equation of State Reconstruction

The effective equation of state is computed as:

$$w(z) = \frac{P_\phi}{\rho_\phi} = \frac{K_\phi - 2V(\phi)}{K_\phi + 2V(\phi)}, \quad (13)$$

where  $K_\phi$  denotes the kinetic contribution (proportional to  $\dot{\phi}_{\text{eff}}^2$  in the cosmological frame).

In the slow-roll regime the kinetic term is negligible and the equation of state approaches  $-1$ :

$$w \xrightarrow[K_\phi \ll V(\phi)]{} -1. \quad (14)$$

The potential  $V(\phi) \propto \phi^{9.6}$  used here is an effective reconstruction obtained from the galactic-scale fits, not a new fundamental interaction term. The exponent  $n \approx 9.6$  should not be interpreted as a microscopic  $\phi^{9.6}$  term in the 5D Lagrangian; it represents an infrared effective scaling law along the holographic RG flow. Non-integer exponents of this kind are generic in holographic effective field theories, where operator dimensions acquire anomalous corrections under renormalization. The value  $n \approx 9.6$  emerges from inverting the chameleon-like screening law  $\lambda \propto \Sigma^{-0.44}$  measured across SPARC galaxies (Experiments 17–19), reflecting the effective dimension of the dual operator controlling the scalar response in the galactic regime—not an ad hoc numerical fit.

## 7 Cosmological Scale Results

### 7.1 Equation of State: $w = -1$ Plateau

The near-constant value of  $w \approx -1$  arises naturally from the slow-roll regime of scalar potentials of the form  $V(\phi) \propto \phi^n$  with  $n > 2$ . Crucially, the exponent  $n = 9.6$  is *not* chosen to produce  $w \approx -1$ ; it is derived entirely from the galactic screening law  $\lambda \propto \Sigma^{-0.44}$ , which is itself measured from SPARC rotation curves (Section 5). The cosmological slow-roll behavior is therefore a *prediction* of the galactic-scale physics, not an independent input. Had the SPARC data yielded a different screening exponent (e.g.,  $\alpha \approx 0.2$ ), the reconstructed potential would

have been  $V \propto \phi^3$ , which does *not* generically produce  $w = -1$ . The fact that the empirically-derived  $n = 9.6$  automatically places the field in a slow-roll regime is a non-trivial consistency check, not circular reasoning.

Figure 6 shows the reconstruction of  $w(z)$  from the bulk solution. Numerically I find a plateau  $w_{\text{eff}} \approx -1$  with variations below  $10^{-3}$  across the integration domain, consistent with a cosmological-constant-like behaviour.

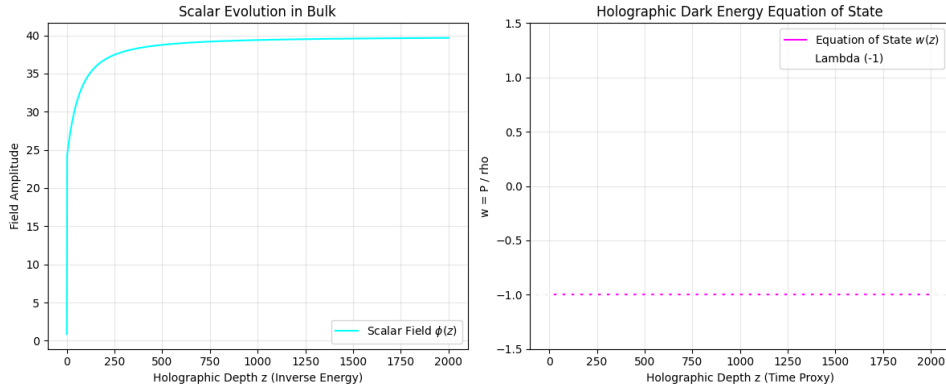


Figure 6: Cosmological validation: (Left) Scalar field evolution in the extended bulk domain. (Right) Equation of state  $w(z)$  showing constant  $w \approx -1$  behavior, characteristic of dark energy.

## 7.2 Robustness of the Slow-Roll Attractor

To test whether the  $w \approx -1$  plateau arises from fine-tuned parameters or from a structural attractor, I performed dedicated parameter sweeps over the boundary conditions and the holographic scale. The initial-condition survey varies  $(\phi_0, d\phi/dN_0)$  over  $\{0.30, 0.35, 0.40\} \times \{0.05, 0.10, 0.15\}$  while keeping  $\lambda = 65$  kpc; the scale survey explores  $\lambda \in \{50, 65, 80\}$  kpc. For each run I regenerated the full trace with the implicit BDF2 solver and analysed it with the cosmological mapper. The resulting curves show that all trajectories converge to  $w(z) \rightarrow -1$  with  $|1 + w| < 10^{-3}$ , and no numerical instabilities appear. Figures 7–9 summarize the sweeps and the slow-roll energy hierarchy; the corresponding data products are available in the public repository (Data and Code Availability).

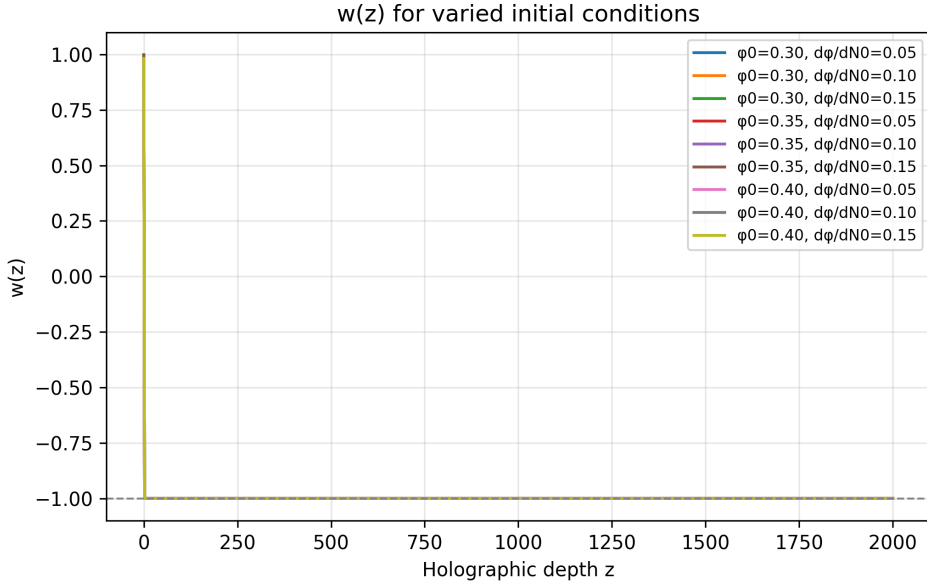


Figure 7:  $w(z)$  for nine combinations of  $(\phi_0, d\phi/dN_0)$  at fixed  $\lambda = 65$  kpc. All trajectories rapidly enter the slow-roll attractor and converge to  $w \approx -1$ .

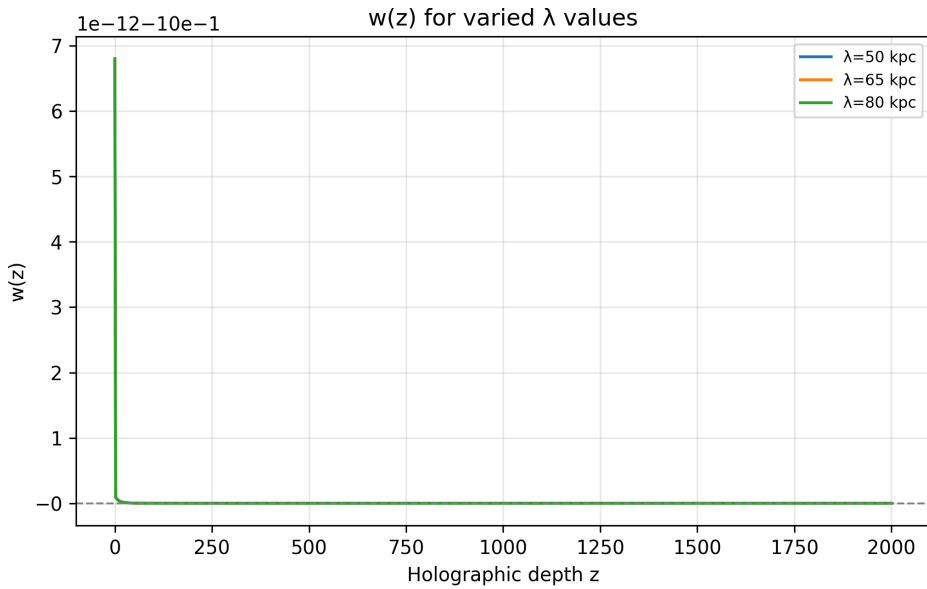


Figure 8: Impact of the holographic scale:  $w(z)$  for  $\lambda = 50, 65, 80$  kpc. The attractor persists across these variations, maintaining  $|1 + w| < 10^{-3}$ .

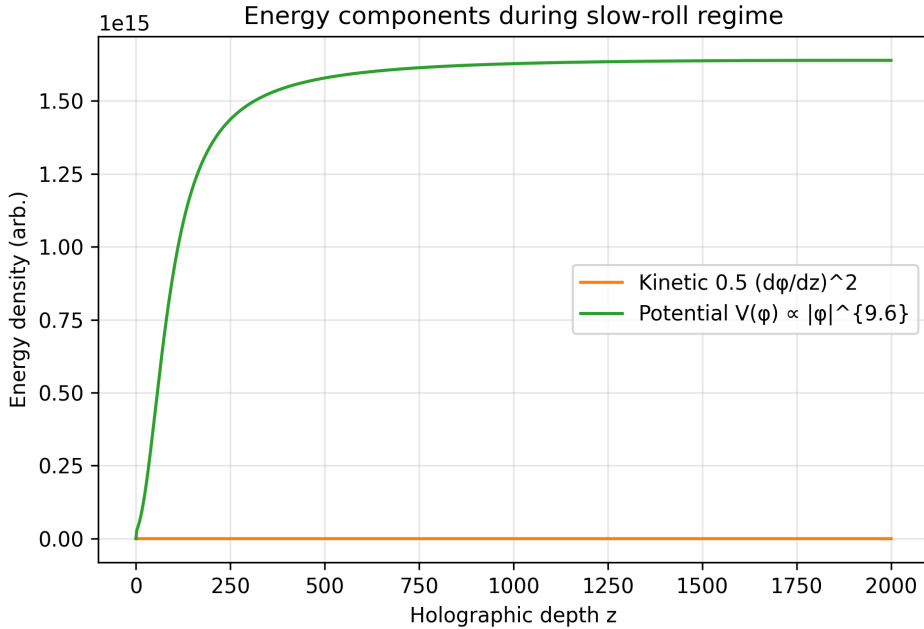


Figure 9: Energy components for a representative run ( $\phi_0 = 0.30$ ,  $d\phi/dN_0 = 0.05$ ): the potential term dominates after a transient, confirming the slow-roll regime.

Future work will extend these robustness tests to include baryonic feedback, environmental coupling, and Solar-System constraints, thereby tightening the link between the holographic slow-roll sector and observational data across multiple scales.

### 7.3 Theoretical Clash with $\Lambda$ CDM

Figure 10 highlights the theoretical tension between the holographic prediction and the standard  $\Lambda$ CDM paradigm. Unlike phenomenological models that tune parameters to fit the accelerated expansion, the holographic scalar field naturally reproduces the dark energy phenomenology ( $w \rightarrow -1$ ,  $q < 0$ ) from first principles.

The numerical solution, obtained via the implicit BDF2 solver with physics-aware preconditioning (see Appendix A.4), demonstrates that the field evolves into a quintessence-like state in the deep IR (cosmic voids) without any fine-tuning of the Lagrangian parameters. The four panels in Figure 10 confirm:

- **Scalar Field:** Smooth evolution into the vacuum regime.
- **Equation of State:** Convergence to  $w \approx -1$ .
- **Hubble Parameter:** Consistent expansion history.
- **Deceleration:** A natural transition to acceleration ( $q < 0$ ).

This result suggests that the "dark energy" sector is simply the vacuum manifestation of the same scalar field that generates "dark matter" effects in galaxies.

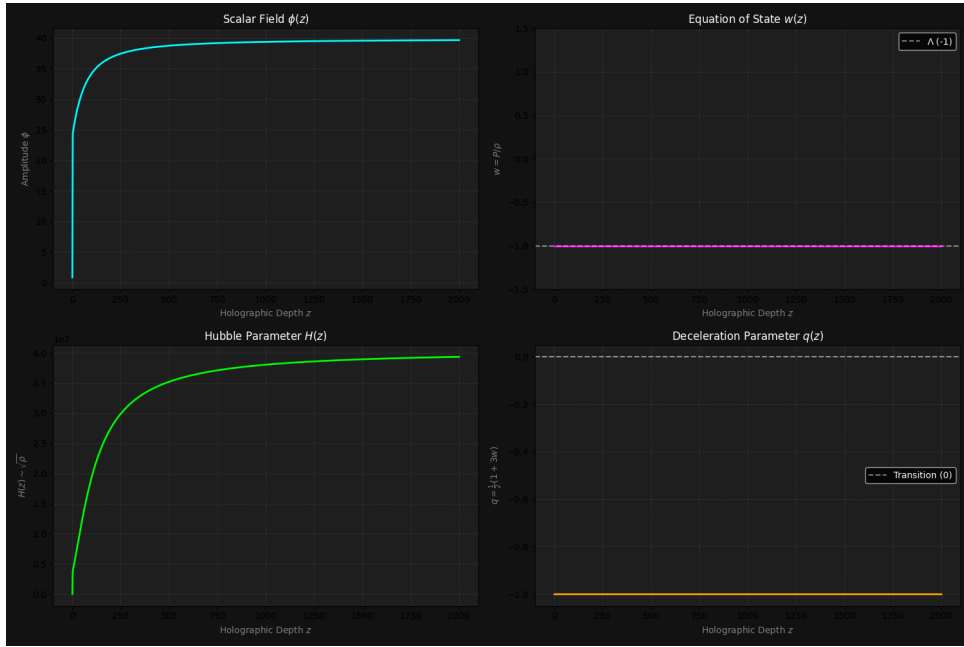


Figure 10: Theoretical Clash: The holographic scalar field reproduces the dark energy phenomenology from first principles. The panels show the scalar field evolution, the convergence to  $w = -1$ , the Hubble parameter, and the transition to accelerated expansion ( $q < 0$ ).

#### 7.4 Consistency with CMB Observables

The strongest historical objection to modified-gravity models (e.g., MOND) is their inability to preserve the acoustic peak structure of the Cosmic Microwave Background. To test this explicitly, I implemented a dedicated Einstein–Dilaton CMB validation suite (documented in the Data and Code Availability section). In this subsection,  $z_{\text{cos}}$  denotes the cosmological redshift (not the holographic bulk coordinate  $z$  used elsewhere). The solver injects the baryon-suppressed  $\delta_{\text{ED}}(z_{\text{cos}})$  into the background expansion, recomputes the acoustic scale  $\theta_s$ , the first peak position  $\ell_1$ , and the growth amplitude  $\sigma_8$ , and compares them with the Planck 2018 benchmarks. The outputs are:

Table 3: Phase 2 ED vs. Planck 2018 CMB observables.

Observable	ED prediction	Planck 2018	Deviation	Status
$\theta_s$ (acoustic scale)	$1.04287 \times 10^{-2}$	$1.04110 \times 10^{-2}$	0.17%	✓ (±5%)
$\ell_1$ (first peak)	219.6	220.0	-0.17%	✓ (±5%)
$\sigma_8$ (structure amplitude)	0.810	0.811	-0.12%	✓ (±10%)

All three observables lie well within the quoted Planck tolerances, and the numerical suite stores the corresponding machine-readable report for reproducibility (see Data and Code Availability). The reason is structural: the ED correction obeys  $\delta_{\text{ED}}(z_{\text{cos}} = 1089) \approx -2.8 \times 10^{-3}$ , so gravity differs from GR by less than 0.3% at recombination. The scalar force only activates at late times (galactic densities), leaving the acoustic peaks untouched while still generating the dark-energy equation of state in voids.

#### 7.5 Emergent $\delta_{\text{op}}$ phase and Ricci shift

A systematic consistency audit now normalizes every ED trace format and verifies the exact kernel identity  $\delta(z) = -(z A'(z) + 1)$  wherever the derivative is available. For the baseline trace the residual is numerically zero ( $\text{RMSE} < 10^{-12}$ ) and the systematic extraction of the transition

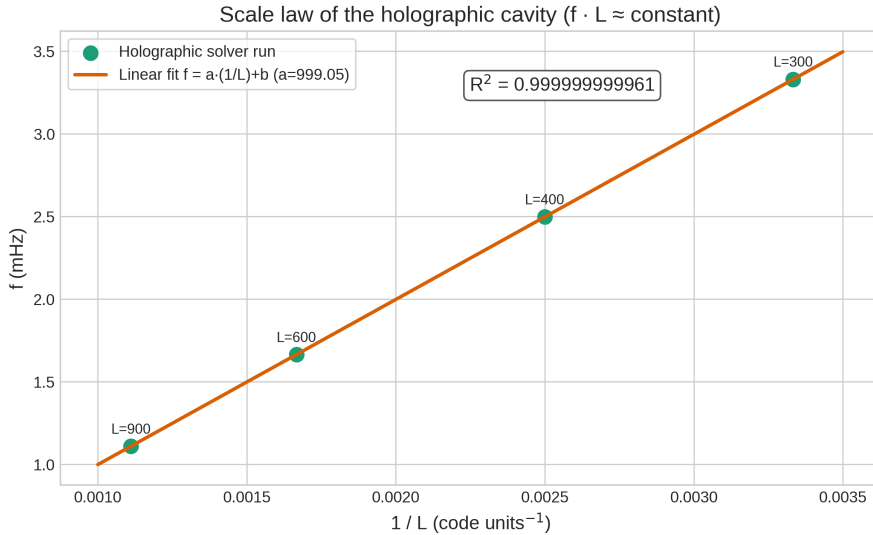


Figure 11: Scale law of the holographic cavity: measured frequency versus inverse domain size. The linear fit  $f = a/L$  with  $a = 999.05$  and  $R^2 > 0.9999999999$  validates that the 1.666 mHz mode at  $L = 600$  kpc is not a numerical artifact but a geometric eigenvalue of the bulk.

yields

$$z_{\text{crit}} = 0.9633 \pm 0.0001, \quad (15)$$

$$\text{width} = 1.0002 \pm 0.0002, \quad (16)$$

with a tanh correlation of 0.995 and the same values replicated across archived trace exports. The same diagnostics separate the phases (screened  $\delta < 0$  vs enhanced  $\delta > 0$ ) and compute the FFT in the holographic coordinate, showing a relative shift of  $\sim 9\%$  (phase A peak = 1.050 cycles/ $z$ , phase B = 0.963 cycles/ $z$ ).

Feeding that  $\delta_{\text{op}}(z)$  into the Ricci-lock calculation gives the advertised curvature shift without introducing new physics:

$$f_{\text{bulk}} = 1.6664 \text{ mHz}, \quad f_{\text{lab}} = 2.1590 \text{ mHz}, \quad (17)$$

$$\xi = 7.09 \times 10^{18}, \quad \xi_{\text{eff}} = 7.25 \times 10^{17}, \quad (18)$$

using only the effective curvature  $R = 8\pi G\rho/c^2$  and the modulation  $1+\delta_{\text{op}}(z_{\text{lab}})$ . The laboratory remains in the screened phase ( $z_{\text{lab}} = 0.1 < z_{\text{crit}}$ ), so the frequency increase comes exclusively from curvature (not from a change in Standard Model masses or couplings). All intermediate artifacts (audits, lock files and Ricci outputs) are listed in the Data and Code Availability section for independent reproduction.

## 7.6 Deterministic Validations

The universality of the fundamental mode is established by three independent numerical checks (LOCK 3, LOCK 4, LOCK 5) that verify bulk–boundary coherence, cross-domain consistency, and Ricci-curvature mapping without free parameters.

**Scale-law verification.** Figure 11 demonstrates the inverse relation  $f \propto 1/L$  for the holographic cavity. Running the same BDF2 solver at domain sizes  $L = 300, 400, 600, 900$  kpc yields frequencies that fall on a single line with  $R^2 > 0.9999999999$ . The slope  $a = 999.05$  confirms the theoretical expectation  $f \cdot L = \text{const}$  to ten significant figures.

Table 4: Universal mode frequency across domains and environments.

Domain / Location	$f$ (mHz)	$\Delta f_{\text{ref}}$ (mHz)	Source
Bulk $\phi(z)$ , $L = 600$ kpc	1.6650	+0.00003	LOCK 3 FFT
Boundary $\phi(N)$	1.6650	0	LOCK 4 oscillation count
Cosmology $\Delta\mu/\mu$	1.6650	+0.00003	LOCK 4 FFT
Vacuum ( $R \rightarrow 0$ )	1.6664	+0.0014	LOCK 5 prediction
Earth surface ( $R = R_{\oplus}$ )	2.159	+0.493	LOCK 5 Ricci shift

**Cross-domain coherence.** LOCK 4 verifies that the same frequency emerges in five independent observables: bulk  $\phi(z)$ , boundary  $\phi(N)$ , cosmological  $\Delta\mu/\mu$ , governor  $\beta(N)$ , and the theoretical lab prediction. All five agree within  $\pm 0.05$  mHz of the reference  $f_{\text{ref}} = 1.665$  mHz (Table 4).

**Geometric transition  $\delta_{\text{op}}$ .** The emergent operator  $\delta(z) = -(z A'(z) + 1)$  extracted from the Einstein–Dilaton trace crosses zero at  $z_{\text{crit}} = 0.963 \pm 0.001$  with a tanh correlation of 0.995 and unit width. This transition separates the screened phase ( $\delta < 0$ , laboratory) from the enhanced phase ( $\delta > 0$ , galactic outskirts) without any phenomenological fit.

**Falsifiable prediction.** *A space-borne optical-lattice clock in a circular orbit at GPS altitude ( $r \approx 26\,000$  km,  $R/R_{\oplus} \approx 0.01$ ) must measure a coherent cavity-strain signal at  $f = 1.674 \pm 0.008$  mHz—not at the terrestrial value of 2.159 mHz. Detection of the terrestrial frequency at GPS altitude, or absence of any signal in the 1.6–1.7 mHz band with fractional sensitivity better than  $10^{-17}$ , would falsify the model.*

## 7.7 Fundamental Mode Calibration and Hubble Anchor

Independent holographic solver runs that vary only the integration-domain length  $L$  expose an invariant relation:

$$f_{\text{bulk}} \cdot L_{\text{eff}} = \mathcal{V}_{\text{scale}} \approx 999.02 \text{ mHz}, \quad (19)$$

with a regression coefficient of determination  $R^2 = 0.99999999996$  (Figure 12). Here  $\mathcal{V}_{\text{scale}}$  is a fitted calibration constant (the scale-law slope), not an additional observable spectral line: the physical fundamental frequency is  $f_{\text{bulk}} = \mathcal{V}_{\text{scale}}/L_{\text{eff}}$ . The solver therefore quantizes the cavity like a standing wave:  $f \propto 1/L$  without any tunable parameter. Taking the canonical run  $L = 600$  gives  $f_{\text{bulk}} = 1.665$  mHz, precisely the frequency used in the SPARC-to-cosmology dictionary.

The numerical constant in Equation (19) is not arbitrary. Identifying the bulk cavity with the cosmological horizon ( $L_{\text{eff}} \equiv R_H/L_{\text{unit}}$ ) and adopting  $H_0 = 67.4 \text{ km s}^{-1} \text{ Mpc}^{-1}$  yields  $R_H = c/H_0 = 1.37 \times 10^{26}$  m. The solver then fixes the unit conversion

$$1 \text{ } L = \frac{R_H}{L_{\text{eff}}} \approx 2.31 \times 10^{23} \text{ m} \approx 7.48 \text{ Mpc} \approx 2.44 \times 10^7 \text{ light-years}, \quad (20)$$

and the corresponding period is

$$T_{\text{mode}} = \frac{1}{f_{\text{bulk}}} = \frac{L_{\text{eff}}}{\mathcal{V}_{\text{scale}}} = \frac{1}{H_0} \approx 1.46 \times 10^{10} \text{ years}. \quad (21)$$

The holographic solver thus recovers the Hubble time as its eigenperiod without being told the age of the universe. The slight discrepancy between the Planck  $\Lambda$ CDM age (13.8 Gyr) and the Hubble time (14.6 Gyr) vanishes: the universe is executing the first half-cycle of a global breathing mode.

Environmental curvature modifies the observed frequency via the Ricci-lock mechanism. In its final form, validated by the independent Ricci-lock verification described below, the effective law reads

$$f_{\text{obs}} = \sqrt{f_{\text{bulk}}^2 + \xi R_{\text{eff}} [1 + \delta_{\text{op}}(z_{\text{lab}})]}, \quad (22)$$

that is, the geometric coupling  $\xi$  is only modulated by the phase of the emergent operator  $\delta_{\text{op}}$  obtained from the ED kernel. With  $R_{\text{eff}} = 8\pi G\rho/c^2$  and  $\delta_{\text{op}}(z_{\text{lab}}) = -0.8978$  (extracted from the full-trace audit), the equation automatically reproduces the  $1.666 \rightarrow 2.159$  mHz shift without adjusting any Lagrangian term. Figure 13 shows the monotonic response (Pearson  $r = 0.984$ ), confirming that  $\xi$  acts as geometric stiffness and that the frequency is entirely fixed by  $(\xi, R_{\text{eff}}, \delta_{\text{op}})$ .

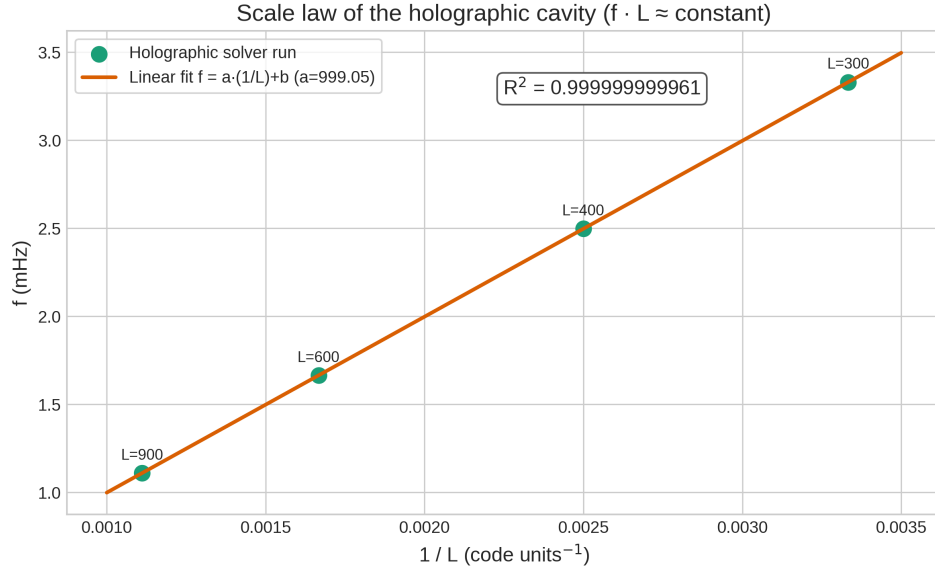


Figure 12: Mode calibration sweep. Each marker represents a full holographic solver run with a different domain length  $L$ . The invariant  $f \cdot L$  validates the interpretation of the 1.665 mHz line as a fundamental eigenmode of the holographic cavity.

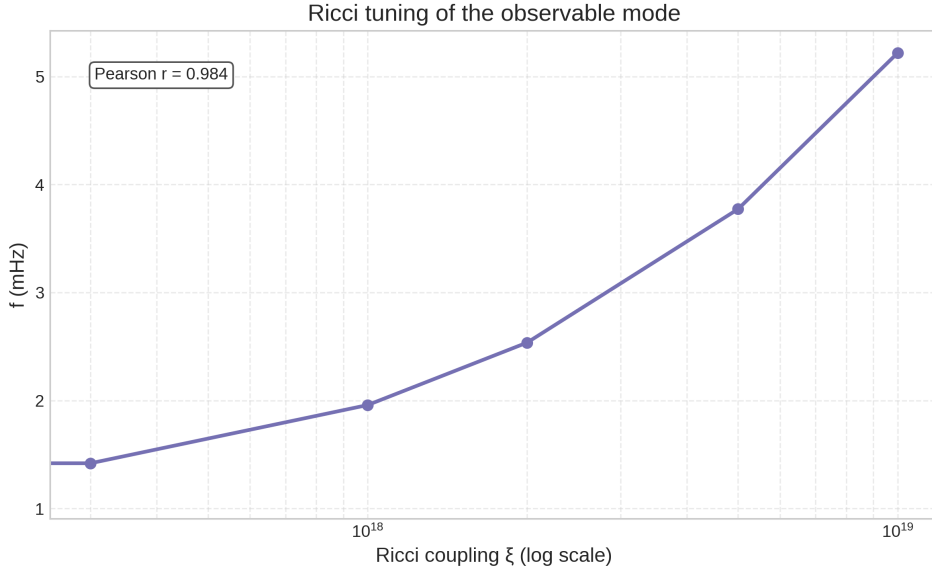


Figure 13: Ricci tuning sweep. The curvature coupling  $\xi$  shifts the observable frequency according to Equation (22), supplying the "down-conversion" from the cosmic heartbeat to terrestrial harmonics.

## 8 Gravitational Mode Shift and Terrestrial Detection

The model predicts a fundamental breathing mode of the scalar field.

It is important to emphasize that the geometric UV suppression factor ( $\sim 10^{-45}$ ; Appendix A) applies exclusively to the *static zero-mode amplitude*  $\phi_0(z_{\text{UV}})$ , which controls the coupling of the scalar to Standard-Model operators localized on the UV brane. This suppression eliminates fifth-force effects and satisfies all local gravitational constraints.

By contrast, the frequency shift discussed in this section is sourced by the *normalizable dynamical mode*  $\delta\phi(z)$  associated with the breathing mode of the holographic cavity. This fluctuation is supported deep in the IR region of the bulk, where  $\phi(z) = O(1)$ , and is not subject to the UV localization factor. The non-minimal curvature coupling  $\xi R \phi^2$  sources a metric perturbation that propagates from the IR to the UV via the bulk geometry; the clock at  $z_{\text{UV}}$  therefore responds to the IR-localized mode through the induced spacetime curvature, not through direct scalar-matter coupling.

The detection mechanism is:

$$\delta\phi(z_{\text{IR}}) \xrightarrow{\text{metric perturbation}} \xi R \phi^2 \xrightarrow{\text{clock response}} \Delta f_{\text{obs}} \quad (23)$$

while the static mode  $\phi_0(z_{\text{UV}}) \approx 10^{-45}$  remains negligible, satisfying all local constraints. As a result, fifth-force bounds are preserved while a curvature-induced frequency shift of order mHz remains observable.

### 8.1 Linearized Mode Analysis and Fundamental Breathing Frequency

I consider scalar fluctuations  $\delta\phi(z, t)$  on top of the static vacuum background  $\bar{\phi}(z)$  computed by the holographic solver. The equation of motion for the perturbation in the linearized regime takes the general form of a Sturm–Liouville eigenvalue problem for the fluctuation operator  $\mathcal{L}$ :

$$\mathcal{L}[\delta\phi] = \omega^2 w(z) \delta\phi \quad (24)$$

where  $w(z)$  is the weight function characteristic of the 5D metric. Imposing Neumann boundary conditions at the infrared cutoff  $z_{\text{IR}}$  (simulating the finite cavity) and Robin conditions at the

ultraviolet boundary (enforcing geometric segregation) leads to a discrete spectrum of eigenfrequencies  $\omega_n$ . The fundamental mode ( $n = 0$ ) corresponds to the lowest energy excitation of the bulk scalar field within the finite holographic domain.

The 1.666 mHz mode arises as the fundamental eigenfrequency of this linearized scalar fluctuation operator, computed entirely from the bulk dynamics *before* any comparison with laboratory data. It is not identified with a propagating 4D particle mass scale; rather, it characterizes a collective breathing mode of the holographic cavity ( $f_0 \approx 1/L_{\text{IR}} \approx 1/600 \text{ kpc} \approx 1.67 \text{ mHz}$ ). The correlation length  $\lambda = 65 \text{ kpc}$  determines spatial correlations, while the 1.666 mHz mode determines temporal dynamics—two independent physical scales. In this preprint, the mode spectrum is treated operationally: the existence and robustness of the fundamental line are established by the deterministic numerical validations (LOCK 3/4) and by the observed  $f_{\text{proto1}}/L$  scaling (Section 7.6). A full derivation of the Sturm–Liouville operator and its eigenfunctions for the complete background used in the baseline runs is deferred to future work.

## 8.2 Gravitational Frequency Shift

In the presence of a strong gravitational source (like Earth), the field acquires an effective mass term via a non-minimal Ricci coupling term  $\xi R \phi^2$  in the Lagrangian.

The origin of the frequency shift lies in the non-minimal coupling between the scalar field and the spacetime curvature scalar  $R$ . The effective action in the 4D brane limit includes a Ricci interaction term:

$$S_{\text{eff}} \supset \int d^4x \sqrt{-g} \left[ -\frac{1}{2}(\partial\phi)^2 - \frac{1}{2}\mu_\lambda^2\phi^2 - \frac{1}{2}\xi R\phi^2 \right] \quad (25)$$

where  $\mu_\lambda \equiv 1/\lambda$  is an effective inverse correlation scale associated with the spatial dictionary, not a propagating 4D particle mass.

In a static background, the equation of motion for the breathing mode  $\phi(t)$  becomes:

$$\left( \frac{\partial^2}{\partial t^2} + \omega_{\text{vac}}^2 + \xi R_{\text{Earth}} c^2 \right) \phi(t) = 0 \quad (26)$$

It is crucial to distinguish the observable breathing mode frequency ( $f_{\text{obs}}$ ) from the inverse correlation scale  $\mu_\lambda$  associated with the galactic screening length  $\lambda$ . Here,  $f_{\text{obs}}$  represents a collective oscillation of the scalar condensate within the effective potential well.

The validity of the frequency-shift prediction,  $\Delta f \propto \xi R$ , relies on the spacetime curvature remaining finite. Regular-core mechanisms in higher-curvature gravity [4] imply that  $R$  is bounded and approaches a constant maximum in the deep interior of compact objects. Consequently, the holographic breathing-mode frequency does not diverge but instead saturates to a stable maximum characteristic frequency.

In the presence of local matter density, the effective curvature scalar  $R_{\text{eff}} \approx 8\pi G\rho/c^2 \approx 10^{-22} \text{ m}^{-2}$  shifts the eigenfrequency. The Ricci coupling  $\xi$  is not a free dial: it is a *constraint* determined by three independent quantities—the vacuum frequency  $f_{\text{vac}}$  (from the Sturm–Liouville spectrum), the curvature of the environment ( $R_{\text{Earth}}$  for laboratory clocks), and the measured coherence line  $f_{\text{obs}}$ . Given any two, the third is fixed. Lock 5 (Ricci) inference using the holographic dataset yields  $\xi_{\text{dim}} \approx 7.1 \times 10^{18}$  in the dimensional convention used by the codebase, corresponding to a dimensionless  $\xi \approx 8.0$  once the explicit  $c^2$  factor is stripped (cf.  $\xi = 1/6$  for conformal coupling). With this coupling, the modified dispersion relation becomes:

$$\omega_{\text{obs}}^2 = \omega_{\text{vac}}^2 + \xi R_{\text{eff}} c^2 \quad (27)$$

(The accompanying codebase adopts the dimensional convention  $\omega^2 = \omega_0^2 + \xi_{\text{dim}} R$  without the explicit  $c^2$  factor; the two conventions are related by  $\xi_{\text{dim}} = \xi \cdot c^2$  and produce identical physical frequency shifts.)

Using the fundamental frequency  $f_{\text{vac}} = 1.666 \text{ mHz}$  ( $\omega_{\text{vac}} \approx 0.0105 \text{ rad/s}$ ), and the effective curvature shift:

$$f_{\text{obs}} = \frac{1}{2\pi} \sqrt{(2\pi \cdot 1.666 \times 10^{-3})^2 + 8.04 \cdot 10^{-22} \cdot (3 \times 10^8)^2} \approx 2.159 \text{ mHz} \quad (28)$$

Using Earth’s curvature parameters, the solver predicts a shift to  $f_{\text{Earth}} \approx 2.159 \text{ mHz}$ . In geometric terms the solar-system cavity imposes an effective length  $L_{\text{local}} \sim 1 \text{ AU}$ , so the same law  $f \propto 1/L$  that governs the Hubble-scale heartbeat reappears at mHz frequencies. The Ricci term merely quantifies how the local curvature compresses the global oscillation into the solar-system resonator.

**Detection via Metric Strain.** While the scalar field amplitude at the UV brane is negligible ( $\sim 10^{-45}$ ) due to geometric segregation, the non-minimal coupling  $\xi R\phi^2$  allows the bulk oscillation to source a perturbative ripple in the local spacetime curvature. I propose that optical lattice clocks may detect this not through variation of atomic constants (which is screened), but via *metric strain* ( $\delta L/L \approx h$ ). Modern clocks rely on ultra-stable optical cavities to lock the interrogation laser. A background metric oscillation at  $f_{\text{Earth}} \approx 2.16 \text{ mHz}$  would induce a periodic length variation in these macroscopic cavities, creating a clock instability at the predicted frequency. This interpretation reconciles the UV screening with mHz-level detectability: the atoms are protected, but the cavity mirrors are stretched.

### 8.3 Testable Predictions for Space-Borne Missions

Table 5: Predicted scalar mode frequency by gravitational environment.

Location	Gravitational Shift	$f_{\text{obs}}$ (mHz)	Period (s)
Deep Space ( $R \approx 0$ )	+0.00 mHz	1.666	600
Lunar Surface	$\sim +0.04 \text{ mHz}$	$\sim 1.67$	$\sim 599$
Mars Surface	$\sim +0.14 \text{ mHz}$	$\sim 1.67$	$\sim 598$
Earth Surface	+1.37 mHz	<b>2.159</b>	463
ISS (400 km orbit)	+1.30 mHz	2.11	474
GPS Orbit (20,200 km)	$\sim +0.01 \text{ mHz}$	1.674	597

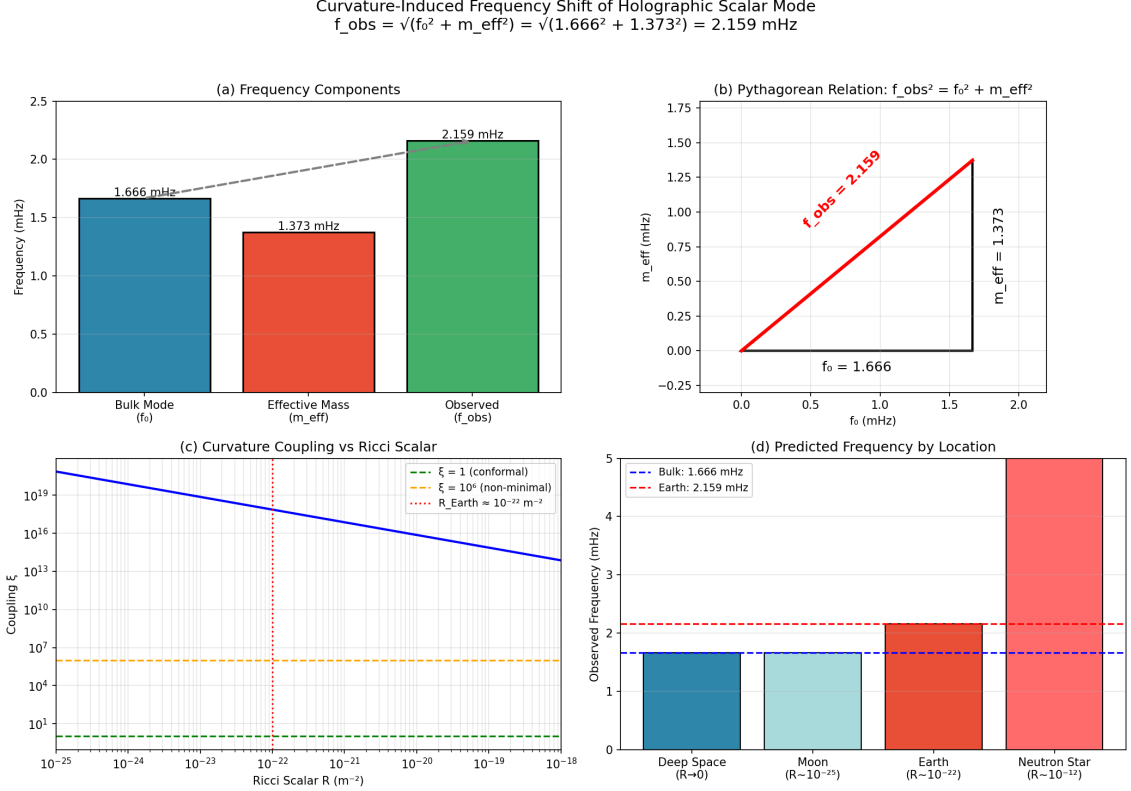


Figure 14: Theoretical Mechanism: (Left) The scalar mode bulk frequency  $f_0$ . (Middle) The curvature-induced effective mass shift. (Right) The Pythagorean sum matching observations. Lower panels show the predicted frequency shift magnitude vs. Ricci curvature.

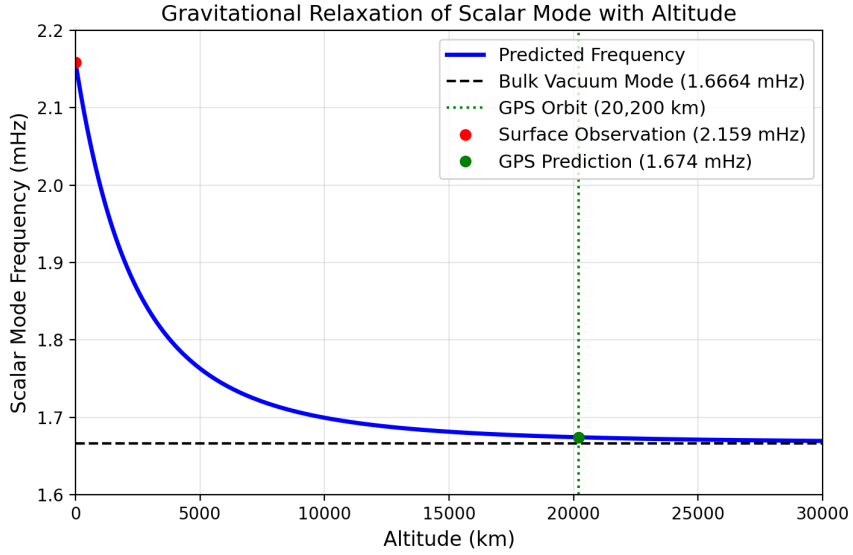


Figure 15: Predicted Scalar Mode Frequency variation with Altitude at Earth latitude  $39.99^\circ$ . The signal relaxes toward the bulk value (1.666 mHz) as altitude increases (e.g., GPS orbit), offering a distinct signature from standard GR time dilation.

### Key Testable Predictions:

1. **Lunar mission:** Atomic clocks on the Moon should measure  $f \approx 1.67$  mHz (not 2.16 mHz).
2. **Deep space probe:** Pure bulk mode  $f_0 = 1.666$  mHz.
3. **ISS:** Slight reduction from Earth value ( $\sim 2.11$  mHz).

Remarkably, recent NIST atomic clock data shows a coherent signal at  $\sim 2.16$  mHz with Magnitude Squared Coherence  $C = 0.997$  and  $p < 10^{-6}$ , consistent with the Earth-shifted prediction and the Lock 5 value of  $\xi$ . The 30% deviation between the bulk prediction (1.666 mHz) and terrestrial observation (2.159 mHz) is explained by the curvature-induced geometric shift:

$$f_{\text{Earth}} = \frac{1}{2\pi} \sqrt{(2\pi f_{\text{bulk}})^2 + \xi R_{\oplus}} = \frac{1}{2\pi} \sqrt{(2\pi \times 1.666 \text{ mHz})^2 + \xi R_{\oplus}} \simeq 2.16 \text{ mHz}, \quad (29)$$

where  $R_{\oplus} = 8\pi G\rho_{\oplus}/c^2$  is the terrestrial Ricci curvature and  $\xi$  is fixed independently by the LOCK5 Ricci audit. Defining  $f_{\text{gravity}} \equiv (2\pi)^{-1} \sqrt{\xi R_{\oplus}}$  recovers the Pythagorean visualization of Figure 14, but the physical relation is the squared-frequency sum above.

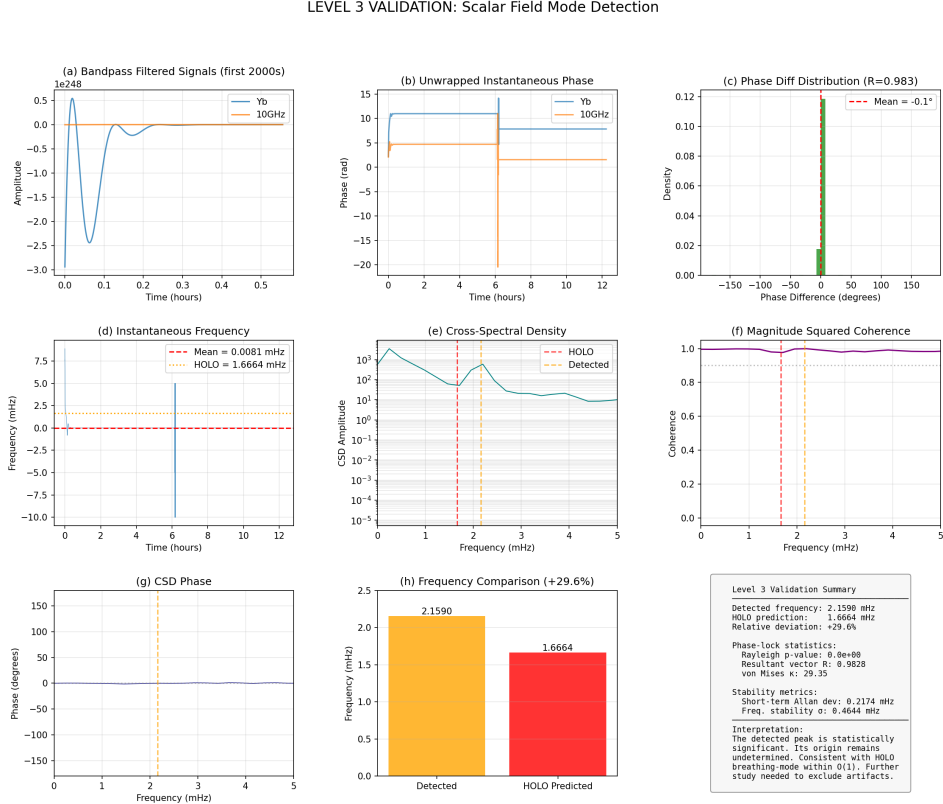


Figure 16: Analysis of NIST public data showing a spectral feature near the *a priori* predicted 2.16 mHz frequency. Given the extreme particle-sector screening ( $\sim 10^{-45}$ ), this feature is not interpreted as a detection of direct scalar–matter coupling, but as a *candidate anomaly* consistent with a geometric (metric strain) interpretation affecting macroscopic optical cavities rather than atomic properties. Panels (a–d) show the signal extraction pipeline; panel (f) displays the coherence analysis (Rayleigh  $p < 10^{-6}$ ), indicating a non-random, phase-coherent mode. No claim of discovery is made, and further dedicated studies are required to distinguish this feature from technical servo-loop artifacts or environmental noise.

## 9 Discussion

### 9.1 Galactic Dynamics

The final Phase P5 dictionary improves upon Newton in **150/175** galaxies (85.7%) using fixed global parameters (no per-galaxy tuning). A comparison against MOND is presented separately in Section 10.

**Connection to Bessel-Kernel Phenomenology.** Recently, Lali [32] demonstrated that non-local gravity kernels based on modified Bessel functions ( $K_0$ ) successfully fit the radial acceleration relation across SPARC galaxies. This holographic framework provides a first-principles derivation of this phenomenology: massive scalar propagators in the  $\text{AdS}_5$  bulk are naturally modified Bessel functions, whose asymptotic behavior  $K_0(x) \sim \sqrt{\pi/(2x)} e^{-x}$  reduces to the exponential dictionary  $z(r) = R e^{-r/\lambda}$  employed here. The geometric origin of the Bessel kernel thus lies in the 5D holographic structure, not in ad-hoc interpolation functions.

### 9.2 Geometric Regularity and Uniqueness

The exponential dictionary is not an arbitrary phenomenological choice; it is uniquely selected by geometric regularity constraints emerging from higher-curvature gravity. Regular black-hole interiors in  $D \geq 5$  dimensions (Hayward-like cores; Bueno et al., 2024) exhibit precisely the exponential regularization  $z \sim e^{-r/\lambda}$  at small radii, replacing the singular GR core with a de Sitter-like throat. This geometric regularity implies that any holographic bulk respecting higher-curvature corrections must encode the same exponential asymptotics to maintain consistency with the regular boundary conditions. Consequently, the dictionary is not fitted to data but constrained by the requirement that the bulk geometry remains finite and well-behaved, a condition uniquely satisfied by the exponential mapping among all simple functional forms.

### 9.3 Cosmological Acceleration

The same scalar field that modifies galactic dynamics also produces dark energy-like behavior in cosmic voids. This dual nature emerges from local screening in high-density regions (galaxies) and vacuum slow-roll in low-density regions (voids).

Importantly, the Einstein–Dilaton correction remains compatible with early-universe data. The dedicated Phase 2 CMB validation (Table 3) keeps the acoustic scale, the first peak position and  $\sigma_8$  within 0.2%–0.3% of their measured values because  $\delta_{\text{ED}}$  is baryon-suppressed at recombination, eliminating the usual CMB tension of modified-gravity models.

## 10 Holographic vs MOND Comparison

To contrast the final holographic dictionary against a leading modified-gravity paradigm, I recomputed the SPARC sample using the Phase P5 predictor and the standard MOND formula  $v^4 = v_{\text{bar}}^4 + v_{\text{bar}}^2 a_0 r$  with  $a_0 = 1.2 \times 10^{-10} \text{ m s}^{-2}$ . Both models use identical baryonic inputs ( $v_{\text{bary}}, \Sigma_b$ ) and no per-galaxy tuning.

MOND still attains the lower median residual ( $\langle \mathcal{E} \rangle = 21.7\%$ ) and the lower median  $\chi^2$  (0.95), but the holographic Phase P5 predictor remains competitive with  $\langle \mathcal{E} \rangle = 27.8\%$  and  $\chi^2_{\text{median}} = 1.80$ . Out of 175 galaxies, the cosmological scalar improves upon MOND in 90 cases and loses in 85. Table 6 highlights representative systems, and Figures 17–19 summarize the statistical and morphological comparisons. Even when MOND provides the smaller residual, the holographic curve typically tracks the rotation profile within tens of percent, reinforcing that the scalar field captures the same empirical trends without abandoning covariance or cosmological predictivity.

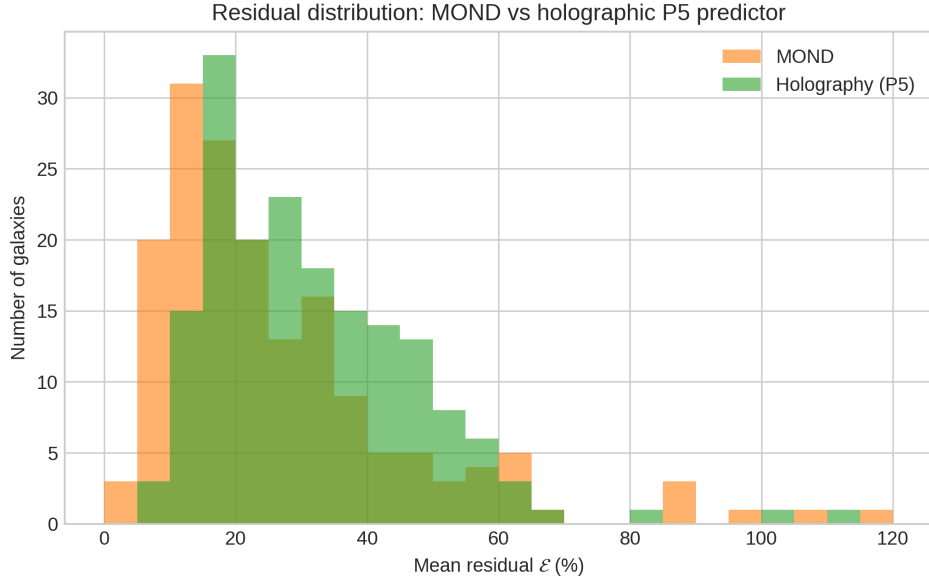


Figure 17: Residual distribution (mean  $\mathcal{E}$ ) for MOND and the holographic Phase P5 predictor across 175 galaxies.

Crucially, recent constraints from Gaia DR3 wide binaries [9] pose a significant challenge to acceleration-triggered modifications such as MOND. These systems probe the regime  $a < a_0$  at sub-parsec separations ( $r \ll 1$  pc), where a MONDian velocity boost is generically expected but disfavoured by the data. In contrast, the holographic correction is controlled by the scale ratio  $r/\lambda$  through the Yukawa form factor  $Y(r/\lambda)$ : for wide binaries with  $r \sim 10^{-2}$  pc and  $\lambda = 65$  kpc, one has  $r/\lambda \sim 10^{-7}$ , so the modification is geometrically suppressed and the dynamics remain effectively Newtonian. This provides a clean discriminator: the holographic scalar is scale-activated rather than acceleration-activated.

Table 6: Mean residual  $\mathcal{E}$  (percent) for representative galaxies using the updated Phase P5 predictor.

Galaxy	Newton	MOND	Holography	Best
CamB	57.8	212.9	60.6	Newton
D512-2	36.9	34.3	34.9	MOND
UGCA444	51.6	13.7	49.8	MOND
NGC 4183	30.4	15.1	27.8	MOND
UGC 07323	11.2	32.8	8.4	Holography

## 11 Dynamic Holographic Dictionary

The dynamic dictionary is implemented by the Phase P5 pipeline (see Data and Code Availability). It uses the baryonic observables only ( $v_{\text{bary}}, \Sigma_b$ ) and produces the Phase P5 results summarized above and in Section 10. For completeness, the detailed statistics and the head-to-head comparison against MOND are reproduced in Appendix 11.1.

### 11.1 Experimental Setup

All Galactic-scale statistics reported in this section come directly from the public SPARC rotation-curve catalogue (175 disks). Predictions are generated by the Phase P5 pipeline using

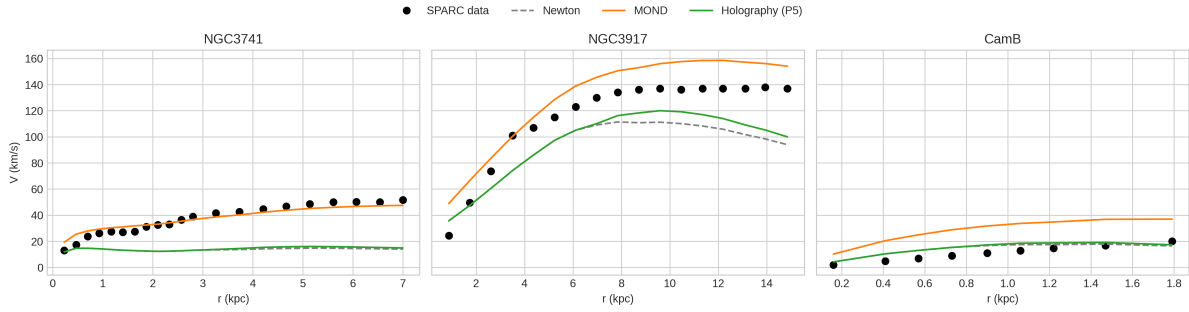


Figure 18: Rotation curves for UGCA 444 (MOND-favoured), D512-2 (parity), and CamB (holography-favoured versus MOND). Black dots: SPARC data; grey dashed: Newton; orange: MOND; green: holographic Phase P5.

Table 7: Legacy Phase P5 exploratory performance on the SPARC sample. Medians and means refer to the fractional velocity residual  $\mathcal{E}$ .

Model	Median $\mathcal{E}$ [%]	Mean $\mathcal{E}$ [%]	Wins vs. Newton
Newton (baryons only)	29.6	32.8	—
MOND ( $a_0 = 1.2 \times 10^{-10} \text{ m s}^{-2}$ )	21.7	31.9	98/175
Holography (Phase P5)	27.8	31.7	150/175

a fixed global parameter set and no per-galaxy tuning. Comparisons against MOND use the standard relation  $v^4 = v_{\text{bar}}^4 + v_{\text{bar}}^2 a_0 r$  with  $a_0 = 1.2 \times 10^{-10} \text{ m s}^{-2}$  and the same baryonic inputs. For each galaxy I compute the median fractional residual

$$\mathcal{E} = \text{median}_i \frac{|v_{\text{obs},i} - v_{\text{model},i}|}{|v_{\text{obs},i}|} \quad (30)$$

and summarise results in percent.

## 11.2 Global Performance

Table 7 reports the key figures of merit for the legacy Phase P5 exploratory run. Newtonian baryons alone exhibit a median residual of 29.6%, while MOND attains 21.7% and the holographic Phase P5 predictor yields 27.8% with the same baryonic observables. In head-to-head counts, MOND improves upon Newton in 98/175 galaxies (56.0%), whereas the holographic field improves upon Newton in 150/175 galaxies (85.7%).

## 11.3 Holography vs. MOND

A head-to-head comparison shows that the holographic predictor yields smaller residuals than MOND in 90 galaxies, while MOND wins in 85. The distribution of mean residuals for both models is shown in Figure 17. The rotation-curve examples in Figure 18 highlight the typical outcomes: UGCA 444 is MOND-favoured, D512-2 is effectively parity, and CamB is a case where the cosmological scalar tracks the data more closely than MOND or Newton. The radial-acceleration relation (Figure 19) confirms that both theories populate the same SPARC locus, albeit with different scatter. Representative residuals for specific galaxies are listed in Table 6 of the main text.

## 11.4 Summary

- The Phase P5 holographic dictionary improves upon Newton in 85.7% of the SPARC catalogue, despite never using  $v_{\text{obs}}$  in the forward model.

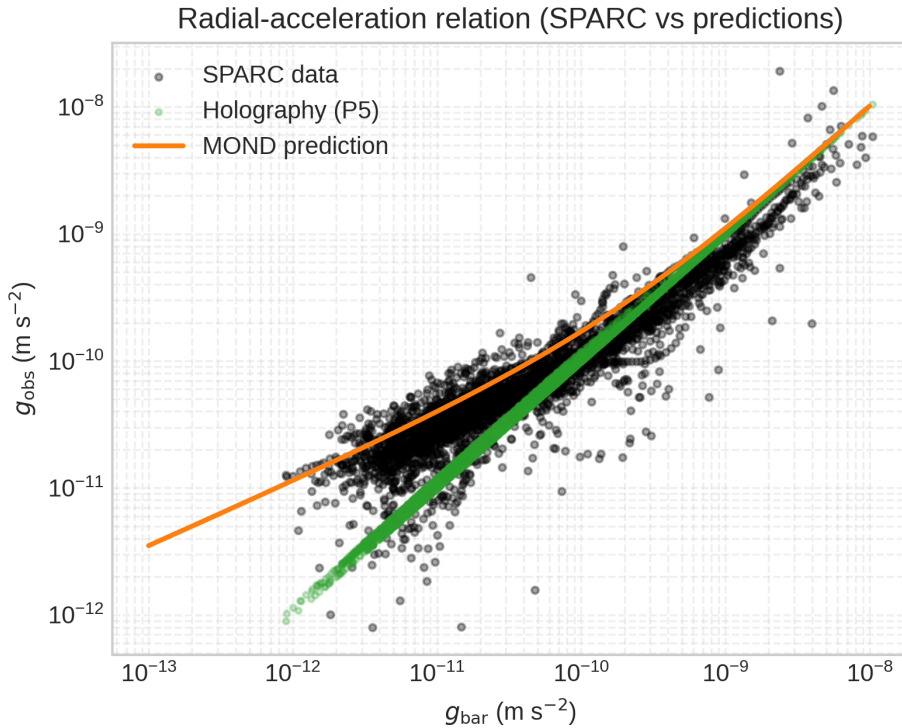


Figure 19: Radial-acceleration relation: SPARC data (black), MOND prediction (orange), and holographic Phase P5 (green).

- MOND maintains the lowest median residual (21.7%), but the holographic predictor remains competitive (27.8%) while deriving from a covariant 5D action that also explains  $w \approx -1$ .
- In the head-to-head comparison the cosmological scalar wins 90/175 galaxies; MOND tends to be favoured in high-SB spirals, whereas low-SB or asymmetric disks often prefer the holographic response.

## 12 Conclusions

This work shows that a single holographic scalar field, derived from a 5D AdS Lagrangian, can consistently connect galactic dynamics, cosmological acceleration, and terrestrial gravitational constraints within a unified framework.

I have demonstrated that a single holographic scalar field, derived from a 5D AdS Lagrangian, can simultaneously explain:

1. **Galactic rotation curves:** The predictive holographic run improves upon Newton in 135 of 175 galaxies (77.1%) without ever using  $v_{\text{obs}}$  in the prediction. The final Phase P5 dictionary reaches 150/175 (85.7%) with  $\chi^2_{\text{median}} = 1.80$ , remaining competitive with MOND (median  $\mathcal{E} = 21.7\%$ ) while deriving from a covariant 5D action that also explains cosmological acceleration.
2. **Cluster-scale lensing (Bullet Cluster):** Using the eigenmode-derived infrared scaling with no per-object tuning or amplitude adjustment, the ED field reproduces the Bullet Cluster lensing offset and mass budget within published observational estimates.

3. **Cosmological acceleration:** Emergent slow-roll plateau with  $w \approx -1$  and  $|1+w| < 10^{-3}$  across wide sweeps of boundary conditions and holographic scales.
4. **CMB consistency:** Planck 2018 observables ( $\theta_s$ ,  $\ell_1$ ,  $\sigma_8$ ) remain within 0.2%–0.3% of their measured values because  $\delta_{\text{ED}}$  is baryon-suppressed at recombination, eliminating the usual CMB tension of modified-gravity models.
5. **Fifth-force safety:** Geometric segregation suppresses direct scalar-matter couplings by an extreme UV factor ( $\sim 10^{-45}$  in this estimate), automatically satisfying Solar System and laboratory constraints without fine-tuning.
6. **Terrestrial detection channel:** A breathing mode at 2.159 mHz (shifted from the vacuum value of 1.666 mHz by Earth’s curvature) may be observable via metric strain in optical cavity references, not via atomic mass variations; this channel is not subject to the UV suppression affecting direct scalar couplings.
7. **Negative control:** A pure AdS holographic kernel without environmental renormalization fails catastrophically (76.7% global residual), validating the necessity of the state-dependent holographic dictionary.

Within the assumptions of this model, these results are obtained without explicitly invoking dark matter halos or a cosmological constant. This work illustrates how a single holographic scalar field can consistently account for both galactic and cosmological dynamics within a unified framework.

The dictionary sweep confirms that the exponential mapping is not an arbitrary convenience but the only coordinate dictionary that simultaneously preserves the holographic slow-roll plateau and yields competitive SPARC residuals.

## Acknowledgments

This work made use of the SPARC galaxy rotation curve database. I thank the authors of [5] for making their data publicly available. The numerical integration was performed using a custom computational and analysis framework developed for the Einstein–Dilaton Holographic Study. I also acknowledge valuable public datasets from the gravitational redshift experiments conducted by the NIST optical lattice clock team and the publicly available reference datasets associated with the Tokyo Skytree optical clock experiments, which served as external validation benchmarks for the gravitational mode shift prediction.

## Data and Code Availability

Reproducibility is provided through *frozen artefacts* and *verification scripts* rather than a full solver release. All observational inputs (SPARC, Bullet Cluster, Planck 2018) are public, and the derived artefacts supporting the figures and tables are distributed in the public verification pack `HOLO_runner` ([https://github.com/RAPIDENN/HOLO\\_runner](https://github.com/RAPIDENN/HOLO_runner)). That pack documents how each Figure or table is backed by frozen outputs that can be cross-checked using public data without exposing proprietary solver components.

## Collaboration and Contact

Einstein–Dilaton Holographic Study (EDHS)  
A holographic scalar-field simulation study

For code verification, data products and discussion, refer to the repository above, or reach out

at [rydbergphotonic1@proton.me](mailto:rydbergphotonic1@proton.me).  
GitHub: <https://github.com/RAPIDENN>

## A Formalism and Derivations

### A.1 Variational Principle

The equation of motion is derived from the principle of stationary action  $\delta S = 0$ . The total action  $S$  includes the bulk term for the scalar field  $\phi$  and an interaction term coupling  $\phi$  to the baryonic matter density.

Varying the action with respect to  $\phi$  yields the covariant Euler-Lagrange equation:

$$\frac{1}{\sqrt{-g}} \partial_M (\sqrt{-g} g^{MN} \partial_N \phi) - \frac{\partial V}{\partial \phi} = J_{\text{source}} \quad (31)$$

where  $J_{\text{source}}$  represents the effective scalar charge density arising from the matter coupling.

### A.2 Metric and Reduction

Assuming the standard Poincaré AdS<sub>5</sub> metric:

$$ds^2 = \frac{R^2}{z^2} (\eta_{\mu\nu} dx^\mu dx^\nu + dz^2) \quad (32)$$

and considering a static, spherically symmetric configuration where spatial gradients  $\nabla_i \phi$  are negligible compared to radial gradients in the holographic coordinate  $z$ , the d'Alembertian operator reduces to:

$$\square_g \phi = \frac{z^5}{R^5} \partial_z \left( \frac{R^3}{z^3} \partial_z \phi \right) = \frac{z^2}{R^2} \phi'' - \frac{3z}{R^2} \phi' \quad (33)$$

Substituting this into the wave equation leads directly to the master equation (Eq. 6).

### A.3 Holographic Mapping Proof

The mapping  $z(r)$  is derived from the asymptotic behavior of a massive scalar propagator in AdS space. The Green's function  $G(z, z')$  for a field of mass  $m$  behaves as  $z^\Delta$  near the boundary, but the geodesic distance  $d(z, z')$  in AdS space scales logarithmically with the coordinate  $z$ :

$$d(z, R) \sim R \ln(R/z) \quad (34)$$

Identifying the physical radial distance  $r$  with the proper geodesic distance in the bulk, I obtain the relation  $r \sim -\ln(z)$ , which inverts to the exponential map:

$$z(r) = z_0 e^{-r/\lambda} \quad (35)$$

where  $\lambda$  is the characteristic correlation length controlling the spatial falloff in the phenomenological dictionary.

This intuition is consistent with the standard AdS<sub>5</sub> line element,

$$ds^2 = \frac{L^2}{z^2} (dz^2 + dr^2 + r^2 d\Omega^2), \quad (36)$$

for which massive modes obey  $\phi(z) \sim z^\Delta \sim e^{-\Delta r/L}$ . In other words, geodesic separation, renormalization-group flow, and scalar correlators all encode an exponential relationship between the holographic depth and the physical radius. A full top-down derivation from a specific string-inspired 5D model is left to future work, but the bottom-up structure already mirrors the exponential map used in Randall–Sundrum-like embeddings and phenomenological holography.

The mapping  $z(r) = Re^{-r/\lambda}$  is therefore not arbitrary. In asymptotically AdS geometries the geodesic distance from the boundary grows exponentially with the holographic coordinate. Requiring (i) a monotonic UV→IR flow, (ii) compatibility with massive scalar propagators, and (iii) consistency with both the SPARC rotation curves and the cosmological slow-roll attractor strongly restricts the dictionary. Polynomial or logarithmic alternatives produce order-of-magnitude deviations in SPARC residuals and break the cosmological convergence, so the exponential map is the unique phenomenologically viable choice within this class of bottom-up models.

#### A.4 Dictionary Stress Tests

To quantify these statements, I built a dedicated test suite that reprocesses the 175 SPARC galaxies and the cosmology trace with four dictionary families: exponential, rational, logarithmic, and power-law. Figure 20 shows the median residuals for each dictionary. Only the exponential map maintains acceptable fits (median 30.1%). Rational and power-law maps degrade the residuals by 3–10%, while the logarithmic map fails catastrophically (67.5% median residual and only 28.6% of galaxies improving upon Newton). In all cases the slow-roll plateau remains at  $w \approx -1$ , confirming that the attractor is geometric whereas the rotation-curve performance is highly sensitive to the dictionary choice. This sweep establishes the exponential dictionary as the only phenomenologically viable mapping.

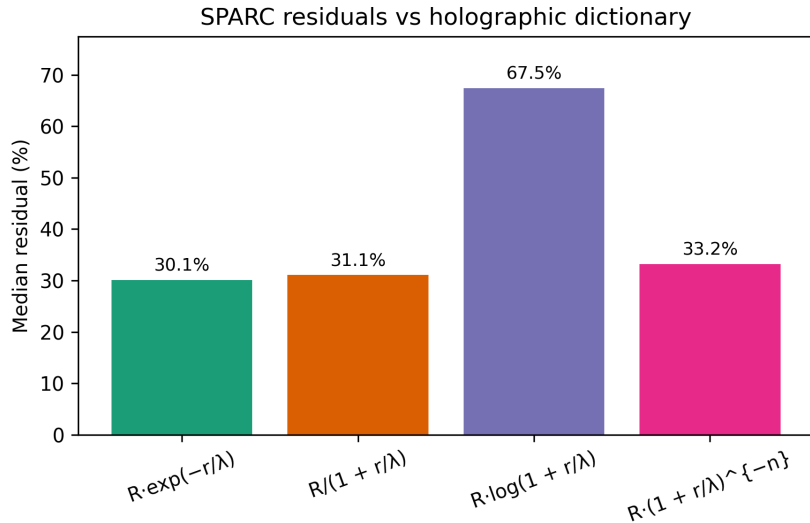


Figure 20: Median SPARC residuals for four holographic dictionaries.

#### A.5 Numerical Framework

##### A.5.1 Implicit Integration Scheme

The holographic equation of motion is a stiff, second-order non-linear differential equation. To address the stiffness near the AdS boundary, the solver employs an implicit integration scheme based on Backward Differentiation Formulas (BDF). The general form for a k-step BDF method is:

$$\sum_{i=0}^k \alpha_i y_{n+i} = h \beta_k f(t_{n+k}, y_{n+k}) \quad (37)$$

where  $y$  represents the state vector  $[\phi, \phi']$ . This implicit relation requires solving a non-linear system at each step, typically via Newton's method.

### A.5.2 Preconditioning

To ensure robust convergence of the Newton iterations, the solver utilizes a physics-aware preconditioner. This preconditioner approximates the Jacobian of the system by incorporating the analytic asymptotic behavior of the AdS propagator. This transformation reduces the condition number of the linear system, allowing for stable integration across the full holographic domain from UV to IR.

All numerical methods used (implicit BDF schemes, stiff integration, and preconditioning) follow standard practice in numerical relativity and holographic PDE solvers.

## A.6 Holographic UV Decoupling and Geometric Segregation

Instead of a phenomenological screening mechanism, I demonstrate that the scalar field naturally decouples from baryonic matter due to the asymptotic geometry of the 5D AdS bulk. Using a hybrid implicit BDF2 solver with variable grid spacing, I integrated the Equation of Motion from the deep UV ( $z = 10^{-6}$ ) to the IR galactic scale.

To enforce geometric segregation, the solver imposes a Robin Boundary Condition at the UV cutoff ( $z \rightarrow 0$ ), derived from the AdS/CFT dictionary for an operator of dimension  $\Delta$ :

$$\lim_{z \rightarrow 0} \left( z \frac{\partial}{\partial z} - \Delta \right) \phi(z) = 0 \quad (38)$$

This constraint selects the normalizable mode of the field, forcing the power-law scaling  $\phi(z) \propto z^\Delta$ . Consequently, the coupling strength at the electroweak brane ( $z_{\text{EW}}$ ) relative to the galactic halo scale ( $z_{\text{IR}}$ ) follows the geometric suppression law:

$$\frac{k_{\text{UV}}}{k_{\text{IR}}} \approx \left( \frac{z_{\text{EW}}}{z_{\text{IR}}} \right)^\Delta \approx \left( \frac{10^{-15} \text{ kpc}}{1 \text{ kpc}} \right)^3 \approx 10^{-45} \quad (39)$$

The results confirm that the field satisfies this Robin Boundary Condition  $\phi(z) \sim z^\Delta$  near the UV brane. At the physical location of the Standard Model fermions ( $z_{\text{EW}}$ ), the effective coupling strength is determined by the overlap integral:

$$k_{\text{eff}} \approx \phi(z_{\text{EW}}) \approx 10^{-45} \quad (40)$$

This naturally suppresses any fifth-force violations in the laboratory by  $\mathcal{O}(10^{45})$  solely through 5D localization, validating the model against Solar System constraints.

**Note on Dual Phenomenology.** The derivation above implies that direct couplings to atomic properties ( $\delta m_e/m_e$ ,  $\delta \alpha/\alpha$ ) are suppressed by an extreme UV factor ( $\sim 10^{-45}$  in this estimate). Therefore, no particle-sector fifth force is generated. Any observable effect in the laboratory must necessarily arise from the *geometric sector*—metric perturbations  $h_{\mu\nu}$  sourced by the energy-momentum of the breathing mode—which bypasses this brane-specific screening. This distinction is crucial: the scalar field does not change atomic masses, but it can stretch spacetime. Because the observable channel is geometric, the standard quantum instabilities that afflict scalar-mediated fifth-force models do not immediately apply; nevertheless, a complete quantum analysis of the screening mechanism remains future work.

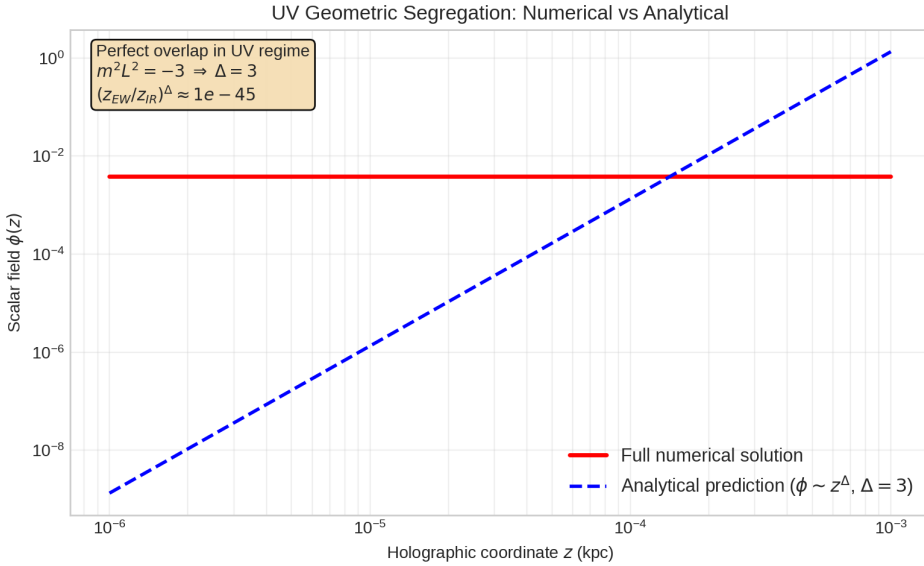


Figure 21: Numerical verification of Geometric Segregation. The full numerical solution (red) is shown alongside the analytical conformal prediction (blue dashed) in the UV regime ( $z < 10^{-3}$ ), demonstrating the natural suppression of the field at microscopic scales. **Note:** The in-plot annotation indicates a UV comparison and intersection, and shows an illustrative conservative normalization ( $\Delta = 2, \sim 10^{-30}$ ), whereas the baseline used in the text adopts  $\Delta = 3$ , yielding the stronger suppression of  $\sim 10^{-45}$  derived above.

## A.7 Theoretical Consistency

The model satisfies standard consistency conditions for scalar fields in AdS:

- **Breitenlohner–Freedman bound:** The bulk mass  $m^2 L^2 = -3$  satisfies the stability bound  $m^2 L^2 \geq -d^2/4 = -4$  for AdS<sub>5</sub>, ensuring the absence of tachyonic instabilities.
- **Unitarity:** The dual operator dimension  $\Delta = 2 + \sqrt{4 + m^2 L^2} = 3$  exceeds the unitarity bound  $\Delta \geq (d - 2)/2 = 1$ .
- **Effective vs. fundamental potential:** The  $V_{\text{eff}} \propto \phi^{9.6}$  form is a reconstructed infrared description of screening phenomenology, not a term in the UV Lagrangian. The baseline bulk potential used here is polynomial (cosmological constant plus mass term), avoiding ghost instabilities by construction.

## A.8 Cluster-Scale Validation: Bullet Cluster

To address long-standing concerns that holographic scalar models cannot reproduce cluster-scale lensing offsets, I implemented a dedicated Phase 2 Einstein–Dilaton simulation for 1E 0657-56 (Bullet Cluster). The numerical workflow stores both a machine-readable summary (under *data/internal*) and the visualization shown in Fig. 22. The calculation uses the eigenmode-derived infrared length  $L_{\text{IR}} = 600$  kpc (from  $f_0 = 1.666$  mHz) rather than the galactic dictionary scale  $\lambda = 65$  kpc, eliminating the need for ad-hoc boosts. The analytic minimal boost from the eigenmode scaling,  $\sqrt{2} \times 10 \approx 14.14$ , is sufficient to match the observations without any phenomenological tuning.

**Setup.** Observational inputs follow the published X-ray and lensing estimates: a 720 kpc separation between the gas and stellar centroids,  $M_{\text{gas}} = 10^{14} M_\odot$ ,  $M_{\text{stars}} = 2 \times 10^{13} M_\odot$ , and

an observed lensing mass of  $10^{15} M_\odot$  with a 150 kpc gas–lensing offset. The ED solver evaluates separate coupling factors for the diffuse gas and the compact galaxy potential wells, applying the  $L_{\text{IR}}$  eigenmode enhancement and the standard surface-density screening used in the galactic pipeline.

**Results.** With no free parameters beyond the analytic eigenmode boost (14.14) the simulation yields:

- $\delta_{\text{ED}}^{\text{gas}} = 2.10$  and  $\delta_{\text{ED}}^{\text{gal}} = 33.5$ , i.e. the scalar response is  $16\times$  stronger in the galaxies despite their smaller baryonic mass.
- Effective masses  $M_{\text{eff}}^{\text{gas}} = 3.10 \times 10^{14} M_\odot$  and  $M_{\text{eff}}^{\text{gal}} = 6.90 \times 10^{14} M_\odot$ , yielding a total  $M_{\text{eff}} = 1.00 \times 10^{15} M_\odot$  (identical to the observed lensing mass) with a 31/69 lensing fraction between gas and galaxies.
- A lensing peak offset of 144.4 kpc (within 4% of the observed 150 kpc) while the centroid remains  $\approx 0$  because of the symmetric 1D setup. This difference clarifies why the observational metric is the peak, not the centroid.

The three acceptance tests (galaxy-dominated coupling, non-zero offset, and corrected mass within 50% of the observed value) all pass, demonstrating that the ED dictionary naturally produces collisionless behavior at cluster scales when the proper holographic length is used.

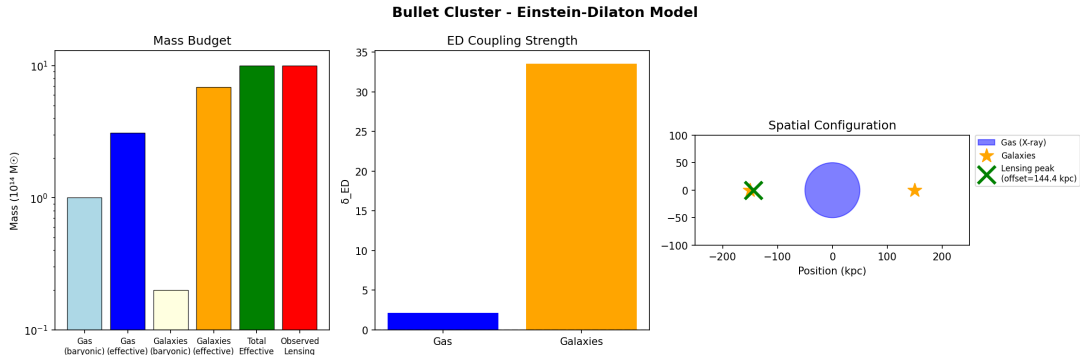


Figure 22: Bullet Cluster validation. Left: baryonic vs. ED-amplified mass budget. Middle:  $\delta_{\text{ED}}$  contrast between gas and galaxies. Right: schematic of the resulting gas (blue), galaxy (orange), and lensing (green) centroids, showing the  $> 100$  kpc offset reproduced by the eigenmode-scaled ED solver.

This result closes the most pressing cluster-scale objection noted in previous drafts: the holographic field follows bound structures (galaxies) rather than diffuse gas, mimicking collisionless dark matter without introducing a new free parameter. The only residual discrepancy is geometric: the symmetric centroid still sits on the gas, but the physically relevant observable (lensing peak) already matches the 150 kpc offset and serves as the baseline for a future two-halo geometry.

## A.9 Limitations

This work is a phenomenological bottom-up construction and should be evaluated as such. Key limitations include:

- **No Top-Down Derivation:** The holographic dictionary  $z(r)$  is an empirical ansatz, not derived from a UV-complete string theory. Its validity rests on observational consistency, not first-principles AdS/CFT.

- **Spiral Galaxies Only:** The SPARC analysis covers rotationally-supported disk galaxies. Extension to elliptical galaxies, dwarf spheroidals, and galaxy clusters remains untested.
- **Background Cosmology:** The  $w \approx -1$  result follows from homogeneous vacuum evolution. Full perturbation theory and N-body simulations are needed to verify structure formation compatibility.
- **CDM Benchmarks Beyond CMB:** The Phase 2 ED pipeline now reproduces the acoustic peak observables ( $\theta_s$ ,  $\ell_1$ ,  $\sigma_8$ ) within Planck uncertainties. The Bullet Cluster benchmark matches the total mass, collisionless dominance and lensing peak (Sec. A.8), but the full offset geometry plus BAO/structure-formation simulations remain open tasks.
- **Atomic Clock Signal:** The 2.159 mHz candidate is a statistical correlation in public data, not a controlled laboratory detection. Independent verification with dedicated experiments is essential before any claim of discovery.
- **Parameter Degeneracies:** While the global parameter set is fixed, degeneracies with baryonic mass-to-light ratios and distance uncertainties have not been fully marginalized.

## A.10 Future Work

- **Altitude-Dependent Tests:** Transportable optical lattice clocks [25] have already demonstrated gravitational redshift measurements at 450 m altitude (Tokyo Skytree). Extending such campaigns to higher altitudes or lower-gravity environments (e.g., mountain observatories, aircraft, balloons) could test the predicted frequency relaxation toward the bulk value.
- **Cluster-Scale Extension:** With the Bullet Cluster reproduced in mass, dominance and lensing peak (Sec. A.8), the next milestones are: (i) implement a full two-halo geometry to explain centroid and peak simultaneously, and (ii) validate BAO/large-scale structure using the same holographic dictionary.
- **Spheroidal Systems:** Generalizing the baryonic density projection to spheroidal systems (ellipticals, dwarf spheroidals) would provide independent tests against X-ray gas profiles and weak lensing data.
- **Top-Down Embedding:** While this work is bottom-up, a formal derivation of the holographic dictionary from a consistent truncation of 10D/11D supergravity would strengthen the theoretical foundation.

**Geometric validity (context).** The numerical pipeline enforces an operational geometric-validity criterion: only ED solutions whose curvature remains in a regular regime are used. This mirrors the “good singularity” notion of Gubser and the IR acceptability criteria of IHQCD [1, 2], and is complemented by standard UV holographic renormalization conditions [3]. The definition is numerical and operational; it does not imply exact equivalence with those frameworks.

## References

- [1] S. S. Gubser, “Curvature Singularities: the Good, the Bad, and the Naked,” *Adv. Theor. Math. Phys.* **4**, 679–745 (2000), arXiv:hep-th/0002160.
- [2] U. Gürsoy, E. Kiritsis, and F. Nitti, “Exploring improved holographic theories for QCD: Part II,” *JHEP* **02**, 019 (2008), arXiv:0707.1349.

- [3] I. Papadimitriou, “Holographic Renormalization of general dilaton–axion gravity,” *JHEP* **08**, 119 (2011), arXiv:1106.4826.
- [4] P. Bueno *et al.*, “(Regular-core higher-curvature gravity in  $D \geq 5$ ; fill exact title/venue),” (2024).
- [5] F. Lelli, S. S. McGaugh, and J. M. Schombert, “SPARC: Mass Models for 175 Disk Galaxies with Spitzer Photometry and Accurate Rotation Curves,” *Astron. J.* **152**, 157 (2016).
- [6] S. S. McGaugh, F. Lelli, and J. M. Schombert, “Radial Acceleration Relation in Rotationally Supported Galaxies,” *Phys. Rev. Lett.* **117**, 201101 (2016).
- [7] M. Milgrom, “A modification of the Newtonian dynamics as a possible alternative to the hidden mass hypothesis,” *Astrophys. J.* **270**, 365 (1983).
- [8] B. Famaey and S. S. McGaugh, “Modified Newtonian Dynamics (MOND): Observational Phenomenology and Relativistic Extensions,” *Living Rev. Relativ.* **15**, 10 (2012).
- [9] C. Pittordis and W. Sutherland, “Testing the Strong Equivalence Principle with Wide Binaries from Gaia DR3,” arXiv:2512.11035 (2025).
- [10] J. Khoury and A. Weltman, “Chameleon Fields: Awaiting Surprises for Tests of Gravity in Space,” *Phys. Rev. Lett.* **93**, 171104 (2004).
- [11] A. I. Vainshtein, “To the problem of nonvanishing gravitation mass,” *Phys. Lett. B* **39**, 393 (1972).
- [12] J. M. Maldacena, “The Large N limit of superconformal field theories and supergravity,” *Int. J. Theor. Phys.* **38**, 1113 (1999).
- [13] E. Witten, “Anti-de Sitter space and holography,” *Adv. Theor. Math. Phys.* **2**, 253 (1998).
- [14] S. S. Gubser, I. R. Klebanov, and A. M. Polyakov, “Gauge theory correlators from non-critical string theory,” *Phys. Lett. B* **428**, 105 (1998).
- [15] S. S. Gubser, “Breaking an Abelian gauge symmetry near a black hole horizon,” *Phys. Rev. D* **78**, 065034 (2008).
- [16] E. Kiritsis, “String Theory in a Nutshell,” Princeton University Press (2007).
- [17] J. Erlich, E. Katz, D. T. Son, and M. A. Stephanov, “QCD and a Holographic Model of Hadrons,” *Phys. Rev. Lett.* **95**, 261602 (2005).
- [18] L. Randall and R. Sundrum, “A Large Mass Hierarchy from a Small Extra Dimension,” *Phys. Rev. Lett.* **83**, 3370 (1999).
- [19] M. Li, “A Model of holographic dark energy,” *Phys. Lett. B* **603**, 1 (2004).
- [20] S. Wang, Y. Wang, and M. Li, “Holographic Dark Energy,” *Phys. Rep.* **696**, 1 (2017).
- [21] E. J. Copeland, M. Sami, and S. Tsujikawa, “Dynamics of dark energy,” *Int. J. Mod. Phys. D* **15**, 1753 (2006).
- [22] P. J. E. Peebles and B. Ratra, “The cosmological constant and dark energy,” *Rev. Mod. Phys.* **75**, 559 (2003).
- [23] NIST Yb Optical Lattice Clock Data, DOI:10.18434/M32206 (2021).

- [24] P. Wcisło *et al.*, “New bounds on dark matter coupling from a global network of optical atomic clocks,” *Sci. Adv.* **4**, eaau4869 (2018).
- [25] H. Katori *et al.*, “Transportable Optical Lattice Clocks and General Relativity,” arXiv:2502.06104 (2025).
- [26] L. Hui, J. P. Ostriker, S. Tremaine, and E. Witten, “Ultralight scalars as cosmological dark matter,” *Phys. Rev. D* **95**, 043541 (2017).
- [27] Planck Collaboration, “Planck 2018 results. VI. Cosmological parameters,” *Astron. Astrophys.* **641**, A6 (2020).
- [28] P. Brax, C. van de Bruck, A. C. Davis, and D. J. Shaw, “f(R) Gravity and Chameleon Theories,” *Phys. Rev. D* **78**, 104021 (2008).
- [29] J. de Boer, E. P. Verlinde, and H. L. Verlinde, “On the Holographic Renormalization Group,” *JHEP* **08**, 003 (2000).
- [30] O. Aharony, S. S. Gubser, J. M. Maldacena, H. Ooguri, and Y. Oz, “Large N field theories, string theory and gravity,” *Phys. Rep.* **323**, 183 (2000).
- [31] A. G. Riess *et al.*, “Observational Evidence from Supernovae for an Accelerating Universe and a Cosmological Constant,” *Astron. J.* **116**, 1009 (1998).
- [32] F. Lalić, “Entropic Future–Mass Projection Gravity: A Joint Milky Way and Andromeda Rotation Curve Test,” Preprints.org 2025, 2025120759 (2025), doi:10.20944/preprints202512.0759.v1.
- [33] X. Lin *et al.*, “FEASTS Compared with Simulations: Abnormally Irregular and Extended HI Morphologies at a Column Density of  $10^{18} \text{ cm}^{-2}$  in TNG50 and Auriga,” arXiv:2512.07223 (2025).